DEPARTMENT OF PHYSICS AND ASTRONOMY
UNIVERSITY OF HEIDELBERG

Master's thesis
in Physics

submitted by

Maximilian David Hartmann
born in Marburg (Germany)

2016

CHARACTERIZATION OF FEW-CYCLE LASER PULSES

This master's thesis has been carried out by
Maximilian David Hartmann
at the
Max-Planck-Institut für Kernphysik
under the supervision of
Prof. Thomas Pfeifer

Characterization of Few-Cycle Laser Pulses—Near-infrared, few-cycle laser pulses are an important tool for state-of-the-art spectroscopy methods. However, their characterization brings about challenges as the femtosecond field transients are out of reach for electronic devices. Therefore, the objective of this thesis is the characterization of such laser pulses by means of two different techniques, namely the dispersion scan and attosecond streaking. Both methods were set up and are—together with the underlying theory—reviewed in detail.

The dispersion scan has the goal of retrieving the spectral phase of the laser pulses by using an iterative algorithm, which was implemented and is evaluated here. Measurement results demonstrate the usefullness of the dispersion scan for day-to-day pulse characterization.

For the attosecond streaking setup with its newly developed design, first test measurements are reported here. The electron time-of-flight spectrometer at the heart of the attosecond streaking setup extends the scope of the existing attosecond transient absorption spectroscopy beamline towards photoelectron studies and the characterization of attosecond pulses from high-order harmonic generation.

Charakterisierung ultrakurzer Laserpulse—Laserpulse mit wenigen optischen Zyklen im nahen infraroten Spektralbereich sind wichtige Werkzeuge für modernste Spektroskopiemethoden. Allerdings erweist sich ihre Charakterisierung als Herausfordergung, da elektronische Hilfsmittel zur Erfassung der wenige Femtosekunden kurzen Lichttransienten nicht genügen. Daher ist es Ziel dieser Arbeit, solche Laserpulse anhand von zwei Methoden, dem Dispersions-Scan und Attosekunden-Streaking, zu charakterisieren. Beide Methoden wurden experimentell umgesetzt und werden hier zusammen mit der zugrundeliegenden Theorie erläutert.

Der Dispersions-Scan gewinnt die spektrale Phase der Laserpulse mit Hilfe eines iterativen Algorithmus, welcher implementiert wurde und hier vorgestellt wird. Anhand von Messergebnissen wird gezeigt, dass der Dispersions-Scan ein nützliches Werkzeug für die alltägliche Lasercharakterisierung darstellt.

Weiterhin werden erste Testmessungen des neu konzipierten Attosekunden-Streaking-Aufbaus vorgestellt. Mit dem Elektronenflugzeitspektrometer, welches das Kernstück dieses Aufbaus ist, werden die Anwendungsmöglichkeiten des bestehenden Experiments zur transienten Absorptionsspektroskopie erweitert hin zu Photoelektronstudien und zur Charakterisierung von Attosekundenpulsen.

Contents

1. Introduction 1

2. Fundamentals 5
   2.1. Ultrashort Laser Pulses 5
      2.1.1. Time and Frequency Domain Relationship 7
      2.1.2. Temporal and Spectral Phase 8
   2.2. Propagation Effects 11
      2.2.1. Dispersion 11
      2.2.2. Non-linear Processes 13
   2.3. The Laser System 15

3. The Dispersion Scan 19
   3.1. Theoretical Background 19
   3.2. The D-Scan Setup 22
      3.2.1. Wedge Alignment 23
   3.3. Phase Retrieval 24
      3.3.1. Spectral Response 25
   3.4. The Downhill Simplex Algorithm 26
      3.4.1. Phase Construction 29
      3.4.2. Convergence Criterion 31
      3.4.3. Initialization 32
   3.5. Evaluation 33
      3.5.1. Consistency Check 34
      3.5.2. Accuracy Tests 39
   3.6. D-Scan Measurements 48

4. Attosecond Streaking 53
   4.1. Theoretical Background 54
      4.1.1. Measurement Principle 56

4.2. The Electron Spectrometer 59
  4.2.1. Spectrometer Design 60
  4.2.2. The Detector 61
  4.2.3. Signal Processing 63
4.3. Experimental Setup 65
  4.3.1. Power Supply 65
  4.3.2. Test Measurements 67

5. Summary and Outlook 69
5.1. Dispersion Scan 69
5.2. Attosecond Streaking 70

A. Appendix i
A.1. Phase Dependence of the D-Scan Trace i
A.2. Supplementary D-Scan Plots iv
  A.2.1. Consitency Measurements iv
  A.2.2. Example D-Scan Characterizations iv

Bibliography xi

1. Introduction

> *The expectations of life depend upon diligence; the mechanic that would perfect his work must first sharpen his tools.*
>
> Confucius

This more than two thousand years old aphorism not only describes an attitude towards life in general, but a key concept of the natural sciences: at the cutting edge of science, persistence and due care are essential. Concerning the study of ultrafast electron dynamics in atoms and molecules, it reminds us to be aware of our tools—the femtosecond laser pulses ($1\,\mathrm{fs} = 10^{-15}\,\mathrm{s}$) used to temporally resolve these dynamics. The shorter the laser pulses are, the better is the time resolution of the experiments and the easier it is to probe strong-field interactions.

However, to be able to sharpen one's tools implies the knowledge of their current state. The difficulty with ultrashort laser pulses is that their shape and structure are not easily measureable. Although their electric field is a quantum mechanical observable, its rapidly varying envelope—let alone the oscillations of the optical carrier wave—changes too fast to be resolved by conventional electronics, which are limited to picosecond time scales ($1\,\mathrm{ps} = 10^{-12}\,\mathrm{s}$). Thus, more evolved characterization techniques for ultrashort laser pulses are indespensable.

As fs-laser-pulses are among the shortest, man-created processes, the trouble of sampling them with an even shorter process is not feasible without the laborious generation of attosecond pulses ($1\,\mathrm{as} = 10^{-18}\,\mathrm{s}$). Instead the interplay of the pulses with a copy of themselves by means of a non-linear process is the common characterization approach. The non-linearity is crucial, because—unlike linear processes—it features the necessary time dependence, whereas the implementation in the form of gating or spectral interferometry varies from technique to technique. Eventually, most techniques resort to the determination of the spectral field—its amplitude and phase—and obtain the temporal pulses by Fourier transformation to the time domain.

Recording the SHG intensity of two time-delay scanned replicas of a pulse with a slow detector yields the intensity autocorrelation, which is the most basic way to get an estimate of the pulse duration. The results of this method cannot be unambiguously inverted and it oversimplifies the temporal structure of the pulses [5], yet it is widely used to get a first estimate of the pulse duration.

Frequency-resolved optical gating (FROG) developed in 1993 by Trebino and Kane [49][27] was the first technique to characterize fs-laser pulses up to their carrier-envelope phase (CEP). It is closely related to the intensity autocorrelation, but instead of measuring just the intensity of a non-linear process, the spectrum for each time delay is captured, which produces a two-dimensional map—a so called FROG trace. This trace is then inverted using an iterative algorithm[8][40] to recover the pulse structure.

Spectral phase interferometry for direct electric-field reconstruction (SPIDER) is the second well established pulse characterization technique for ultrashort laser pulses. It was devised in 1998 by Iaconis and Walmsley [23] and is a non-linear interferometric method. It has the advantage that the phase is retrieved in a non-iterative manner, but it is much more sensitive to misalignment due to several interferometer arms.

By now, FROG and SPIDER have been extended to single shot [30][28] and spatially resolved methods and their working principles have been adapted to characterize sub-fs pulses from high-order harmonic generation (HHG) light sources as well. Some of these variants go by the names of Grenouille[41], Sea-Tadpole[3], Sea-Spider[31], Rabbitt[38] and Frog-Crab[34], just to mention a few.

A more recent technique called *multiphoton intrapulse interference phase scan* (MIIPS)[33; 52; 6] employs a pulse shaper as a tool for pulse characterization. By recording the dependence of a SHG signal on different superimposed phase masks, the GDD of the pulses is approximated and refined by means of an iterative measurement procedure. The principle of using phase variations for pulse characterization is addressed in this thesis, as it is the basis of the dispersion scan technique as well.

The dispersion scan (short D-Scan) is a pulse characterization technique developed by Miranda et al. [37][36] in 2012. The key concept of this approach is utilizing optical elements which are already in the beam path—a pair of glass wedges for dispersion control—and a non-linear response of the pulses to deduce their spectral phase. The glass introduces a variation of the spectral phase, which can then be retrieved by an iterative algorithm.

Differing substantially from the methods described above, attosecond streaking directly accesses the electric field, or more precisely the vector potential of fs-laser-pulses [19]. It does so by measuring the phase-dependent, accelerating effect of the laser field on electrons generated by photoionization of atoms by means of an attosecond pulse. The electrons are detected with a time-of-flight spectrometer. While this work focuses on the characterization of the laser field, such a spectrometer is the heart of several established techniques for the characterization of extreme ultraviolet (XUV) radiation from HHG. There are the *attosecond steak camera* [24] or *atomic transient recorder* (ATR) [29] for the characterization of isolated attosecond pulses and the *reconstuction of attosecond beating by interference of two-photon transitions* (RABBIT) [38], which is used to measure the spectral phase between individual harmonics in trains of attosecond pulses. A more general technique, which encompasses the latter two, is *frequency-resolved optical-gating for the complete reconstruction of attosecond bursts* (FROG CRAB) [34]. In principle, all of these techniques rely on the signature of a cross correlation between the strong driving field and the attosecond excitation field [32] and were inspired by older correlation techniques [9; 21].

The goal of this work was to design and construct a fully functional D-Scan setup for the characterization of our laser system on a day-to-day basis. This included the implementation and optimization of a phase retrieval algorithm. Moreover, an attosecond streaking setup was conceived and constructed. In addition, first test measurements were performed and are reported here.

This work gives a short introduction to the theoretical treatment of ultrashort light pulses, before turning to the presentation of the D-Scan and the attosecond streaking methods and the respective setups. Both techniques are introduced in theory and measurement data is presented. The phase retrieval algorithm of the D-Scan is reviewed in detail and evaluated.

Conventions

Throughout this work, the angular frequency ω of the electric field is often referred to as frequency. In many plots, the spectrum is plotted over the photon energy $\hbar\omega$ instead of the frequency ω without explicit notice.

2. Fundamentals

This thesis deals with the characterization of ultrashort laser pulses where ultrashort means durations below 10 fs (1 fs $= 10^{-15}$ s). Therefore, this chapter gives an introduction to the mathematical description of such pulses in the temporal as well as in the spectral domain in section 2.1 and describes their behaviour upon propagation in section 2.2. Finally, the technical section 2.3 presents the laser system generating the pulses.

2.1. Ultrashort Laser Pulses

The space and time dependent electric field $\mathbf{E}(t, \mathbf{x})$ contains all information to fully describe electromagnetic radiation. Here, the focus lays on the temporal structure of laser pulses. Assuming invariant, linear polarization during propagation and fixing our view at a fixed point in space, we can omit the vectorial character and the spatial dependence of the electric field and simplify our investigation by studying the scalar quantity $\mathcal{E}(t)$.

As mentioned in chapter 1, the electric field is in principle directly accessible and thus, a real quantity. It is related to the spectral field $\mathcal{E}(\omega)$ in the frequency domain via Fourier transform where ω is the angular frequency:

$$\mathcal{E}(\omega) = \frac{1}{\sqrt{2\pi}} \int_{-\infty}^{\infty} \mathcal{E}(t) e^{-i\omega t} \mathrm{d}t, \tag{2.1}$$

$$\mathcal{E}(t) = \frac{1}{\sqrt{2\pi}} \int_{-\infty}^{\infty} \mathcal{E}(\omega) e^{i\omega t} \mathrm{d}\omega. \tag{2.2}$$

To facilitate calculations, $\mathcal{E}(t)$ and its associated spectral counterpart $\mathcal{E}(\omega)$ are commonly replaced by the complex quantities $E(t)$ and $E(\omega)$, which are refered to as the *analytic signals* [2] of $\mathcal{E}(t)$ and $\mathcal{E}(\omega)$. The same Fourier relationship as in equations 2.1 and 2.2 holds for the analytic signals as well and the real valued electric field can always be recoverd by rejecting the imaginary part of the analytic signal:

$$\mathcal{E}(t) = 2\,\mathrm{Re}[E(t)]. \tag{2.3}$$

The complex functions $E(t)$ and $E(\omega)$ still fully characterize the shape of a laser pulse and can be rewritten in terms of amplitudes and phases, both of which will be discussed in more detail below:

$$E(t) = A(t)e^{i\phi(t)}, \tag{2.4}$$

$$E(\omega) = A(\omega)e^{i\varphi(\omega)}. \tag{2.5}$$

Averaging over one optical period T the intensity of an ultrashort laser pulse (in W/cm^2) is defined as:

$$I(t) = \epsilon_0 cn\frac{1}{T}\int_{t-T/2}^{t+T/2} \mathcal{E}^2(t')\mathrm{d}t', \tag{2.6}$$

$$\approx 2\epsilon_0 cnA^2(t), \tag{2.7}$$

where ϵ_0, c and n are the dielectric permittivity, the vacuum speed of light and the refractive index of the propagation medium. The last equality (eq. 2.7) holds only under the assumption that the temporal amplitude envelope $A(t)$ is slowly varying compared to oscillations of the electric field:

$$\left|\frac{\mathrm{d}}{\mathrm{d}t}A(t)\right| \ll \frac{2\pi}{T}\left|A(t)\right|. \tag{2.8}$$

While $I(t)$ is primarily a theoretical quantity, most pulse characterization techniques rely on the time-averaged measurement of the spectral intensity $S(\omega)$:

$$S(\omega) = 2\epsilon_0 cn|E(\omega)|^2, \tag{2.9}$$

$$= 2\epsilon_0 cnA(\omega)^2. \tag{2.10}$$

As equation 2.10 shows, the spectral phase $\varphi(\omega)$ is lost during the measurement and with it crucial information about the pulse shape. Chapter 3 will deal with exactly this problem and is devoted to the recovery of the spectral phase.

2.1.1. Time and Frequency Domain Relationship

We have seen that the functions describing the electric field in the time and in the frequency domain are related via a Fourier transform (equations 2.1 and 2.2). What concequences does this have and what kind of information can one infer from this?

Common measures for the pulse duration and the spectral bandwidth are the full width of the intensity functions at half their maximum value (FWHM) in their respective domain. Here, they shall be abbriviated by Δt_{FWHM} for the pulse duration and $\Delta\omega_{FWHM}$ for the spectral width. Because of the *similarity theorem* of the Fourier transformation [17], there is an inverse relationship between Δt_{FWHM} and $\Delta\omega_{FWHM}$. Similar to the uncertainty principle of quantum physics, this leads to the *time-bandwidth product*, which is defined as:

$$\Delta t_{FWHM}\Delta\omega_{FWHM} \geq 2\pi c_B, \tag{2.11}$$

where c_B is a constant, which depends on the pulse shape $A(t)$. Consequently, ultrashort light pulses have to be supported by broadband spectra. When the equality above holds, the pulses are as short as possible provided a given spectrum and are said to be *bandwidth-limited* or *(Fourier-) transform-limited* (FTL). This case is met when the spectral phase is flat wherever $A(\omega)$ is non-zero, which can be understood as all frequency components, which make up the pulse, oscillating in phase.

As an example, which is also illustrated in figure 2.1, one can consider a normalized, Gaussian pulse in the time domain with standard deviation σ:

$$A(t) = \frac{1}{\sqrt{2\pi}\sigma}\exp\left(-\frac{t^2}{2\sigma^2}\right). \tag{2.12}$$

Using eq. 2.1 the corresponding spectral amplitude can be calculated:

$$A(\omega) = \exp\left(-\frac{\sigma^2\omega^2}{2}\right). \tag{2.13}$$

The pulse duration and spectral bandwidth of the intensity functions (eqs. 2.7 and 2.10) can now be related to the standard deviation of these gaussian functions:

$$\Delta t_{FWHM} = \sqrt{4\ln 2}\,\sigma, \tag{2.14}$$

$$\Delta\omega_{FWHM} = \frac{\sqrt{4\ln 2}}{\sigma}. \tag{2.15}$$

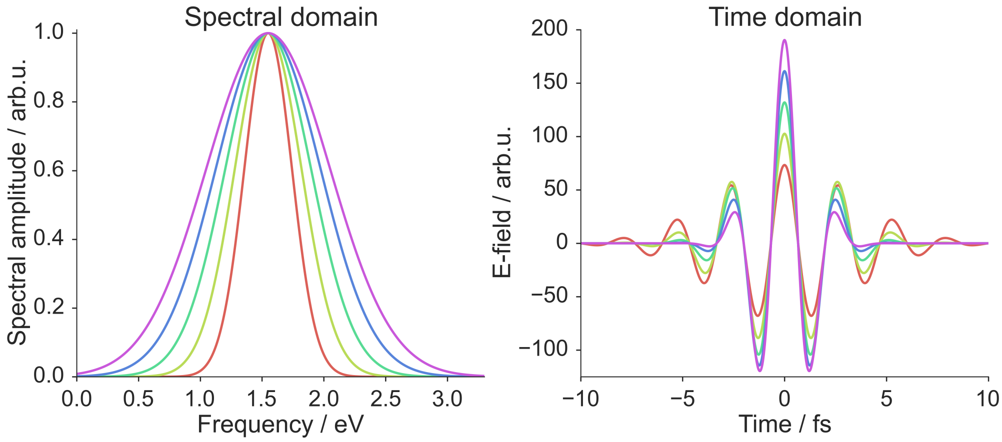

Figure 2.1.: Gaussian pulses in the spectral and time domain. With increasing width of the spectral amplitude (left) the pulses represented by their electric field (right) become shorter and reach higher field strengths.

Thus, for gaussian pulses the time-bandwidth product is always larger than $2\pi c_B = 4\ln 2 \approx 2.77$.

2.1.2. Temporal and Spectral Phase

The time-bandwidth product (eq. 2.11) states that a broad spectrum is needed to support a short laser pulse; but a given broad spectrum does not automatically lead to short light pulses. This has to do with the temporal and spectral phases $\phi(t)$ and $\varphi(\omega)$, which will be examined in the following.

First $\phi(t)$ is expressed as a Taylor series:

$$\phi(t) = \sum_{n=0}^{\infty} \frac{\phi_n}{n!}\, t^n = \phi_{CEP} + \omega_c t + \Phi(t). \tag{2.16}$$

Here, ϕ_{CEP} is a constant phase which causes a slip between the oscillations of the electric field with carrier frequency ω_c and the peak of the amplitude function. Therefore the name *carrier-envelope phase* (CEP). The carrier or center frequency ω_c is not unambiguously defined. When performing the Fourier transformation into the frequency domain (eq. 2.1) it leads to a shift of ω_c to zero because of the *Fourier shift theorem* [17]. It is often assigned to the frequency of the peak of the spectrum or defined as a weighted average of all spectral components. $\Phi(t)$ contains all higher phase orders ($n \geq 2$). Their effect becomes more intuitive by studying the instantaneous frequency of the pulses. The instantaneous frequency $\omega(t)$ of an oscillation is defined as the time derivative of the temporal phase:

$$\omega(t) = \frac{\mathrm{d}}{\mathrm{d}t}\phi(t) = \omega_c + \frac{\mathrm{d}}{\mathrm{d}t}\Phi(t). \tag{2.17}$$

If the phase has only linear terms $\Phi(t)=0$, $\omega(t)$ is constant and the frequency does not change over the duration of the pulse. For $\Phi(t) \neq 0$ the pulse is said to be *chirped.* If the frequency increases/decreases with time, the pulse is called up-chirped/down-chirped. In general, a chirp increases the time-bandwidth product of a pulse (see equation 2.11). Thus, the spectrum of a chirped pulse would support a shorter pulse duration, if it was not for the chirp. Propagation in media imprints a chirp upon pulses depending on the material properties. This leads to the lengthening of FTL pulses and will be addressed in section 2.2.1.

The spectral phase $\varphi(\omega)$ can be expanded into a Taylor series as well:

$$\varphi(\omega) = \sum_{n=0}^{\infty} \frac{\varphi_n}{n!}\,\omega^n = \varphi_{CEP} + \tau_0\omega + \mathit{\Phi}(\omega). \tag{2.18}$$

The first four orders of this expansion and their effect on the electric field are depicted in figure 2.2. The constant term φ_{CEP} is equal to the temporal phase offset ϕ_{CEP}. τ_0 is the pulse's absolute position in time and $\mathit{\Phi}(\omega)$ contains all higher phase orders ($n \geq 2$). Similar to the instantaneous frequency in the time domain, the group delay is defined as the derivative of the spectral phase with respect to frequency:

$$\tau(\omega) = \frac{\mathrm{d}}{\mathrm{d}\omega}\varphi(\omega) = \tau_0 + \frac{\mathrm{d}}{\mathrm{d}\omega}\mathit{\Phi}(\omega). \tag{2.19}$$

The group delay states a relative time delay of the spectral components which make up the pulse. Thus, the linear term in eq. 2.18 corresponds to a delay of all frequency components by $-\tau_0$, but has no effect on its shape. Any higher phase orders ($\mathit{\Phi}(\omega) \neq 0$) introduce a frequency-dependent delay of different spectral components, which eventually smears out the pulse. The first contribution to $\mathit{\Phi}(\omega)$, φ_2 goes by the prominent name of *group-delay disperison* (GDD). Higher orders ($\varphi_3, \ldots$) are simply refered to as *third-order dispersion* (TOD), and so on.

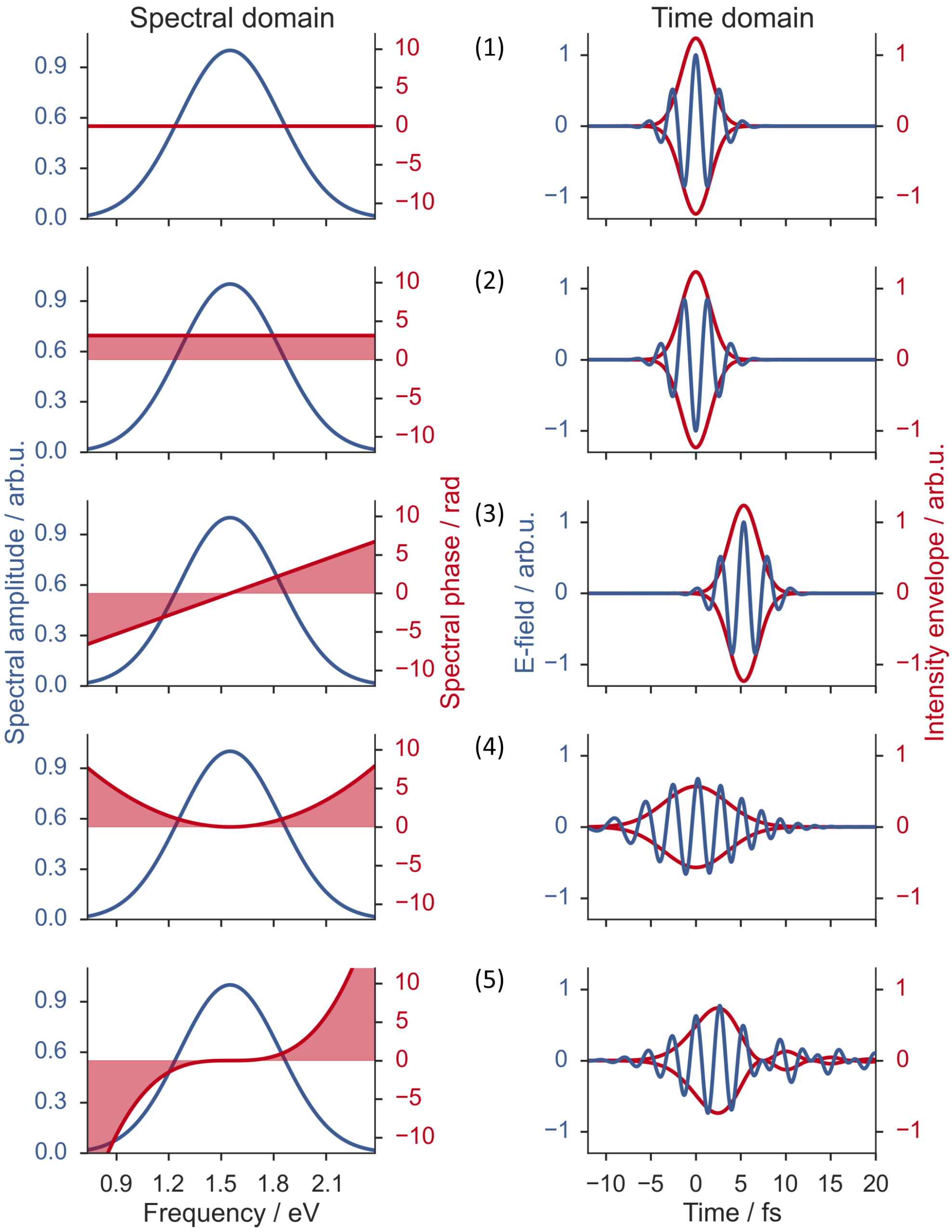

Figure 2.2.: Illustration of the effect of different spectral phase orders (left) on the electric field in the time domain (right). Top to bottom: (1) $\varphi(\omega) = 0$: Fourier transform-limited pulse. (2) Constant phase $\varphi_{CEP} = \pi$: phase-shift of the electric field with respect to its envelope. (3) Linear phase : the pulse's absolute position in time is shifted. (4) Quadratic phase : the pulse is up-chirped, less peaked and longer. (5) Cubic phase : chirp causes post-pulses.

2.2. Propagation Effects

To study the propagation of ultrashort laser pulses in matter, we turn to the wave equation for the electric field $\mathbf{E}(t, \mathbf{x})$ in homogeneous media without currents and charges derived from Maxwell's equations:

$$\left(\boldsymbol{\nabla}^2 - \frac{1}{c^2}\frac{\partial^2}{\partial t^2}\right)\mathbf{E}(t, x, y, z) = \mu_0 \frac{\partial^2}{\partial t^2}\mathbf{P}(t, x, y, z). \tag{2.20}$$

The polarization $\mathbf{P}$ accounts for the response of the medium. For convenience, it can be split into the linear and a non-linear contributions $\mathbf{P}^L$ and $\mathbf{P}^{NL}$:

$$\mathbf{P} = \mathbf{P}^L + \mathbf{P}^{NL}. \tag{2.21}$$

The linear polarization accounts for dispersion, which will be discussed for the case of some standard optical elements in the following section 2.2.1, while the non-linear polarization is the source of exotic processes, which go beyond the superposition principle of linear optics, and will be discussed in section 2.2.2.

As for the spatial dependence of the electric field, which has to be taken into account in the following, plane waves propagating in z-direction in a medium with wave vector $k(\omega)$ are assumed as a solution to equation 2.20:

$$E(\omega, z) = A(\omega, 0) \exp\Big(i\big(\varphi(\omega) - k(\omega)z\big)\Big). \tag{2.22}$$

2.2.1. Dispersion

In transparent optical elements[1], such as lenses and prisms (and air), dispersion is governed by the index of refraction of the material, which is linked to the wave vector via

$$k(\omega) = n(\omega)\frac{\omega}{c}. \tag{2.23}$$

If the refractive index is monotously increasing with frequency ($\mathrm{d}n/\mathrm{d}\omega \geq 0$), the dispersion is said to be *normal*, as is the case for most transparent materials e.g. glasses. In case $\mathrm{d}n/\mathrm{d}\omega < 0$, the dispersion is said to be *anomalous*. As a result of dispersion, the wave vector is usually not a linear function in frequency. By plugging equation 2.23 into equation 2.22, we see that dispersion results in a

---

[1] Losses through reflection and absorption are neglected by the treatment here, which implies that the transmitted amplitudes have no frequency dependence.

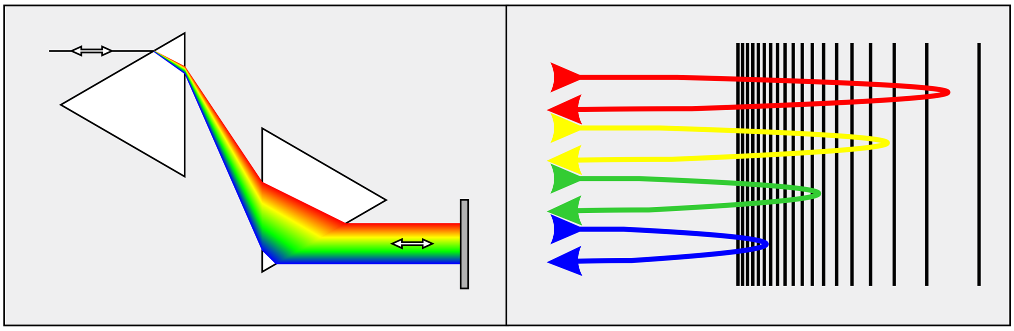

Figure 2.3.: Schematics of a two-prism prism compressor (left) and single chirped mirror (right). In both cases, the high spectral components (blue) have an effectve shorter optical path than the lower ones (red).

phase modification of the propagating pulse. For instance, on a pulse with flat spectral phase, the non-linearity of the wave vector introduces higher-order phase terms, which eventually lead to a chirp. In normal-dispersive materials the low frequency components of the pulse traverse the medium faster than the high frequency components, which causes an up-chirp.

In order to keep ultrashort pulses as short as possible, dispersion control is crucial in fs-laser-systems. Since more positive dispersion can always be added to the pulses by inserting more glass into the beam, the more challenging task is to introduce *negative* dispersion in order to compensate those dispersive elements, which cannot be omitted. The usual approach to achieve this is to arrange optical elements in a setup that has an effective shorter pathway for higher frequency components and causes a down-chirp. Several optical elements are suited to fulfill this function (see also figure 2.3):

Prisms and **Gratings** exhibit angular dispersion which can be employed to build pulse compressors in a variety of arrangements.

Chirped mirrors (CM) are special dielectric mirrors composed of thin multi-layer stacks, which can be designed to have a desired frequency-dependent penetration depth.

2.2.2. Non-linear Processes

Before the invention of the laser in 1961, no light sources in the optical range were available with field strengths high enough to drive non-linear processes. Since then, especially pulsed lasers with high peak intensities have revealed many such processes, some of which rendered the generation and characterization of even shorter light pulses possible. It is because of the latter that certain non-linear processes will be discussed in the scope of this thesis.

Starting out from the wave equation 2.20, we expand the polarization $\mathbf{P}(t)$ in a Taylor series of the incident field:

$$\mathbf{P}(t) = \epsilon_0 \big(\chi^{(1)} \mathbf{E}(t) + \chi^{(2)} \mathbf{E}(t)\mathbf{E}(t) + \chi^{(3)} \mathbf{E}(t)\mathbf{E}(t)\mathbf{E}(t) + \dots \big). \tag{2.24}$$

The different $\chi^{(n)}$ are the n^{th}-order susceptibilities and are in general tensors of order $n+1$. The linear term with $\chi^{(1)}$ is responsible for dispersion (see sec. 2.2.1). The first non-linear effect to be demonstrated [13] was the process of *second-harmonic generation* (SHG), which $\chi^{(2)}$ is responsible for. As the name states, it converts two photons with energy $\hbar\omega_0$ to one photon with twice the energy $\hbar\omega_{SHG} = 2\hbar\omega_0$. To reach macroscopic second-harmonic yield, the participating photons have to conserve momentum as the fundamental and harmonic have to propagate in phase within the medium:

$$\mathbf{k}_{SHG} = \mathbf{k}_{0,1} + \mathbf{k}_{0,2}. \tag{2.25}$$

If this phase matching, which in terms of the refractive index is equivalent to $n(\omega_{SHG}) = n(\omega_0)$, is not fulfilled, the microscopic contributions to the SHG signal across the generation medium interfere destructivly. For a given frequency, phase matching can for example be fulfilled in birefringent crystals with the fundamental and harmonic having different polarizations. But since the wave vectors are frequency dependent $\mathbf{k}(\omega)$, equation 2.25 can in reality not be strictly satisfied for broadband, ultrashort laser pulses. By resorting to extremly thin crystals, the phase-matching condition can be relaxed at the cost of conversion efficiency.

The third-order non-linearities induced by $\chi^{(3)}$ cause (besides other effects) the propagation medium to exhibit an intensity-dependent refractive index:

$$n(\mathbf{r}, t) = n_0 + n_2 I(\mathbf{r}, t). \tag{2.26}$$

This is the so called optical Kerr effect, which is the source of *self-focusing* and *self-phase modulation* (SPM).

In self-focusing, the time- and space-dependent refractive index $n(\mathbf{r}, t)$ creates a lensing effect, due to the spatial intensity profile of the laser beam. This is made use of in fs Ti:sapphire laser oscillators. The Kerr effect inside the laser crystal now benefits high-power pulsed operation over cw operation by inducing fewer losses per cavity round-trip on high intensity pulses. This technique is called Kerr lens mode-locking, because it locks all supported cavity modes in phase in order to build up the shortest possible pulse with the highest peak intensity. Since it uses no active element, it is a passive mode-locking technique.

Self-phase modulation is a process that leads to spectral broadening, because of the temporal-dependence of the refractive index. As the latter is connected to the wave vector, it enters into the temporal phase. By analysing the instantaneous frequency (eq. 2.17) while assuming a gaussian intensity function $I(t) = I_0 \exp\big(-(t/\tau)^2\big)$,

$$\begin{aligned}\omega(t) &= \omega_c - \frac{\omega_c}{c}\frac{\mathrm{d}}{\mathrm{d}t}n(t), &(2.27)\\ &= \omega_c + \frac{\omega_c}{c}\frac{2I_0 n_2}{\tau^2}t\mathrm{e}^{-(t/\tau)^2}, &(2.28)\end{aligned}$$

we see that the leading/trailing edge of the pulse generates new frequency components lower/higher than ω_c. The pulse is now chirped but has a broadened spectrum and can subsequently be compressed to shorter pulse durations.

Up to this point, the general theory laid out here pointed mainly to the description of fs-laser-pulses out of a commercial laser system. Yet it is also applicable to coherent radiation from a process called *high-harmonic generation* (HHG). While SHG and SPM are merely two-/three-photon processes, several dozen of photons can be involved in HHG. Since non-linear polarization cannot account for it, the origin of HHG could not be explained until 1993, when Corkum [7] proposed a semi-classical three-step model, which is sketched in figure 2.4. Irradiating a gas target with a driving field whose peak field strength approaches the order of magnitude of the binding field of the target atom's electrons, some electrons may tunnel out of their binding potential (I). Once freed, they are accelerated by the intense driving field (II) and have a chance to recombine with the parent ion (III). Upon recombination the binding energy plus the excess kinetic energy is released as a high-energetic HHG photon. Macroscopic bursts of HHG radiation are only generated by the peaks of the driving field and are therefore confined to an even shorter time scale than the fs-pulse. Because HHG radiation is located in the extreme ultra-violet (XUV)

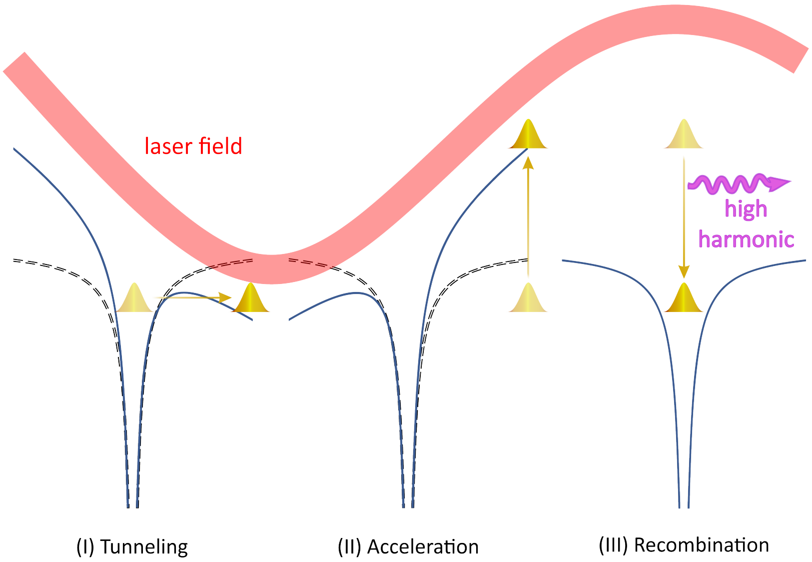

Figure 2.4.: Illustration of the three step model of high-harmonic generation. The laser field (red) bends the atomic potential, which allows some electrons (yellow) to tunnel free (step I). As the laser field passes, its slope changes sign and the electrons are accelerated back towards the atomic core (step II), where they have a certain chance to recombine with the parent ion. The excess energy is released as a high energetic photon (step III).

spectral region, it is strongly ionizing and is absobed by any gas. In order to use this radiation in experiments, beamlines containing parts for the generation, the experiments and optics are operated under vacuum. Further information on the beamline, which was extended by the electron time-of-flight spectrometer presented in chapter 4, and its principal components can be taken from [42].

2.3. The Laser System

The main objective of this thesis is the characterization of fs-laser-pulses provided by a commercial , amplified and externally compressed laser system consisting of a Femtopower Compact Pro CEP, a Kaleidoscope hollow-core fibre (both from the company Femtolasers) and an additional home-built chirped-mirror compressor (PC70, Ultrafast Innovations). The whole setup is depicted in figure 2.5. The seed pulses are generated by a Rainbow CEP3 Ti:sapphire

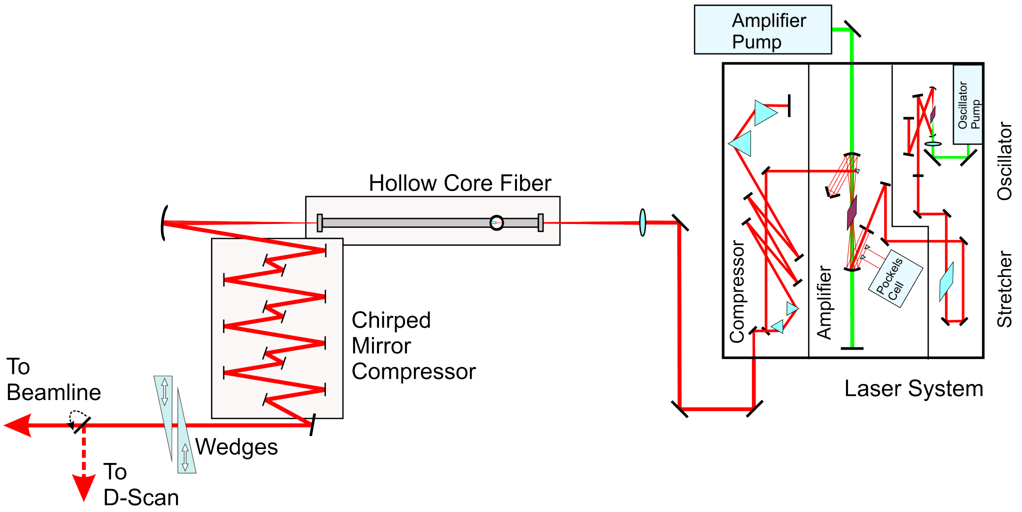

Figure 2.5.: Schematic of the whole laser system. Seed pulses are produced in the oscillator, pass the stretcher and enter the multipass amplifier, where a Pockels cell picks out every 20000^{th} pulse to be amplified further in a 9^{th} pass through the amplifier crystal. Subsequently the pulses are compressed by a prism compressor with four additional TOD mirrors. They are spectrally broadend in a 1 m hollow-core fibre filled with neon and recompressed by a chirped-mirror compressor. After passing the pair of motorized wedges, a flip mirror mount can be used to couple the pulses either into a HHG beamline or into the D-Scan (see chapter 3) for characterization.

oscillator[2] at 78 MHz repetition rate, 2 nJ pulse energy, 780 nm central wavelength and < 10 fs pulse duration. These pulses are subsequently stretched in a glass slab and amplified in a *chirped-pulse amplification* (CPA) stage[48]. The stretching is necessary in order to avoid damage to the amplifier crystal (also Ti:sapphire) and is compensated after the amplification to some extent by a prism compressor (see section 2.2.1) and TOD mirrors. After the compression the pulses have 0.7 mJ pulse energy at 4 kHz repetition rate and < 30 fs duration.

In the CPA stage the pulses are amplified most efficiently around the center of their spectrum, which is called gain narrowing and leads to longer pulse durations. To broaden the spectrum again, the laser beam is focused into a 1 m long hollow-core glass fibre with a core diameter of 250 µm filled with neon at a pressure of ~2.5 bar. The gas of choice is neon, because of its high ionization threshold and large $\chi^{(3)}$, which induces SPM (see equation 2.27) along the

---

[2] The CEP stabilisation was dismounted in this particular oscillator.

length of the fibre. After the fibre the pulses are compressed in a chirped-mirror compressor to compensate for the linear dispersion and non-linear chirp the pulses suffer while propagating in the neon.

The chirped-mirror compressor originally consisted of 5 pairs of broadband double-angle chirped mirrors. During this thesis it was expanded to 7 pairs in order to precompensate for more dispersive optics. Losses from the fibre and the CMs reduce the pulse energy to ~0.38 mJ. With a pair of glass wedges (Femtolasers, material nBK7, apex angle 8°) flexible dispersion control is achieved in order to deliver pulses with durations below 6 fs.

3. The Dispersion Scan

The dispersion scan (short D-Scan) is a pulse characterization technique, which makes use of the pair of glass wedges for dispersion fine-tuning in the laser's beam path and the change of a non-linear spectral signature that is introduced by the phase the glass adds to the pulses upon moving. An iterative algorithm extracts the spectral phase from the measurement data and together with the fundamental spectrum the temporal shape of the pulses is then obtained by Fourier transformation (equation 2.2).

This chapter presents the D-Scan constructed as part of this thesis. The theoretical background and the setup are introduced in sections 3.1 and 3.2. While the experimental part of the D-Scan is a staightforward measurement, quite some effort has to be put into the phase retrieval, which is illustrated in section 3.3. Section 3.4 is devoted to the explanation of the iterative algorithm, which is at the heart of the phase retrieval . The algorithm is evaluated in section 3.5 in order to demonstrate its capabilities. Finally, examples of few-cycle pulse characterization measurements are shown in section 3.6.

3.1. Theoretical Background

In the experimental setup of the D-Scan presented here, the laser pulses pass two glass wedges and a SHG crystal[1] before their second-harmonic spectrum is measured. For the phase retrieval it is crucial for this to be described by an analytic expression, which will be derived in the following:

We start off with the spectral electric field $E(\Omega)$. In first order, the effect of glass on the laser electric field can be treated as a multiplicative phase factor, which depends on the length z and the dispersion of the material (see equation 2.22). Second-harmonic generation is best treated in the time domain by simply squaring the temporal E-field, while the spectral intensity $S(\omega)$ (equation 2.9)

---

[1] D-scans may work best with SHG, but are not limited to this non-linearity. Third-harmonic generation (THG) has been shown to work as well [22].

is recorded in the spectral domain, which makes Fourier transforming back and forth between the two domains necessary. Thus, the SHG spectral intensity measured by the spectrometer as a function of the amount of glass is—in a perfect world—proportional to the following expression:

$$S(\omega, z) \propto \left| \int_{-\infty}^{\infty} \left(\int_{-\infty}^{\infty} E(\Omega) e^{izk(\Omega)} e^{i\Omega t} \mathrm{d}\Omega \right)^2 e^{-i\omega t} \mathrm{d}t \right|^2 . \tag{3.1}$$

This is the two dimensional D-Scan trace, as it will be called in the following.

There is no straightforward way to invert this formula, but some insight can already be gained by analyzing it. For this purpose different D-Scan traces, which were simulated for pulses with varying spectral phase, are shown in figure 3.1. For the simulation of a trace $S(\omega, z)$, the spectral field $E(\Omega)$ is composed according to equation 2.5 of an amplitude, which is either measured or modeled as a Gaussian and a desired phase function. The frequency dependence of the wave vector $k(\Omega)$ is calculated by means of the refractive index, which in turn is given by the Sellmeyer equation of the specific glass of which the wedges are made from. The glass insertion z is sampled such that all of the trace's features around the strongest SHG signal are visible, which is in practice determined by the experiment.

Even without the simulation, we can understand the origin of the shape of the traces. Because a chirped-mirror compressor overcompensates the pulses with negative dispersion, they reach the wedges with a high down-chirp. For low amounts of glass insertion z the dispersion in the glass does not suffice to fully recompress the pulses. This leads to comparatively weak peak intensites and SHG signals from these long pulses. With increasing glass insertion, the pulses reach a point of optimal compression corresponding to the strongest SHG yield, before the signal fades out again, because too much glass insertion has left the pulses up-chirped. This illustrates how the D-Scan is sensitive to variations in the spectral phase (through glass insertion) and that it can be used not only for characterization of the pulses, but to find the wedge position of optimal pulse compression as well.

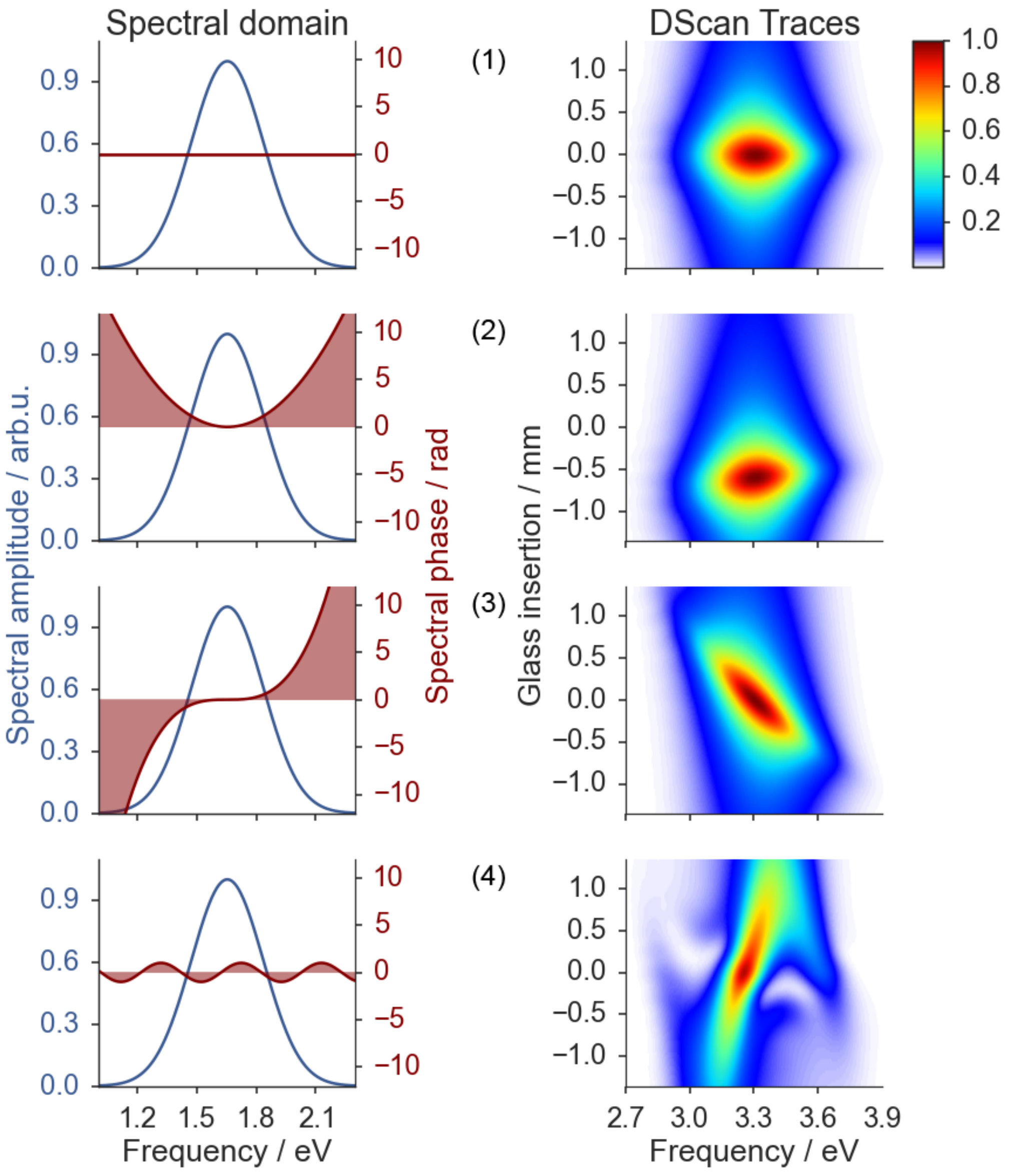

Figure 3.1.: Laser pulses in the spectral domain (left) and their respective D-Scan traces (right, colorbar shows SHG intensity in arbitrary units). Top to bottom: (1) A pulse with flat phase produces an elliptical trace. (2) The quadratic phase mimicks the behaviour of the glass' dispersion, which shifts the trace on the y-axis, and additionally introduces a small tilt. (3) A pulse with cubic phase is easily recognized by the strong tilt of its D-Scan trace. (4) Small amounts of sinousoidal phase ripples as for example introduced by misaligned chirped mirrors distort the trace substantially.

3.2. The D-Scan Setup

A sketch of the D-Scan setup is shown in figure 3.2. First the laser pulses from the chirped-mirror compressor propagate through a pair of BK-7 glass wedges (Femtolasers) with AR-coating and an apex angle of 8°. Each wedge is mounted on a 25 mm linear stage, each of which is equipped with a Conex TRA25CC actuator (Newport) controlled by a standard PC. These servo actuators have a stepping accuracy of 10 µm, well below the precision needed here. By means of a flip mirror mount, the beam can be coupled into the rest of the D-Scan setup mounted on a single breadboard with $30 \times 60\,\mathrm{cm}^2$ footprint. The non-linear crystal used in this setup is a 5 µm thick BBO (β-Barium Borate) from Newlight Photonics. The crystal has to be as thin as this, to relax the phase matching condition for SHG sufficiently in order to facilitate broadband harmonic yield. To reduce damage on the crystal, the SHG is driven by the front reflex of a wedged glass window only (~ 0.4 W), which is focused into the crystal by a concave mirror with 40 cm focal length. The light which passes the wedge is picked up by a screen and the diffuse reflection is captured by one arm of a bifurcated fibre (Ocean Optics) in order to record the fundamental spectrum. In front of the wedged window, a thin pole blocks the central part of the beam to enable non-collinear SHG. The generated second-harmonic light is coupled into the other arm of the bifurcated fibre by means of two aluminium mirrors and a fused silica lens. Scattered fundamental light is filtered out as well as possible using spatial filtering and a thin polarizing foil[2]. The bifurcated fibre is coupled into a high resolution, broadband spectrometer from Ocean Optics (HR4000CG-UV-NIR).

A D-Scan measurement consists of recording SHG spectra in dependence of the amount of glass insertion. Usually, 100 spectra are recorded in order to get a finely sampled trace. Between the acquisition of two spectra, the wedges are alternately moved further into the beam, until each has been inserted by 50 steps of 0.2 mm. Due to the small apex angle of the wedges, this effectively corresponds to additional 2.76 mm glass in the beam path.

Because only one end of the fibre should be employed at once in order to avoid saturation of the fundamental, when the second harmonic is recorded, mechanical shutters are installed before both ends of the bifurcated fibre. These

---

[2] BBO crystals are birefringent, which enables phase matching between the fundamental and the harmonic by having them travel through the crystal with orthogonal polarisations.

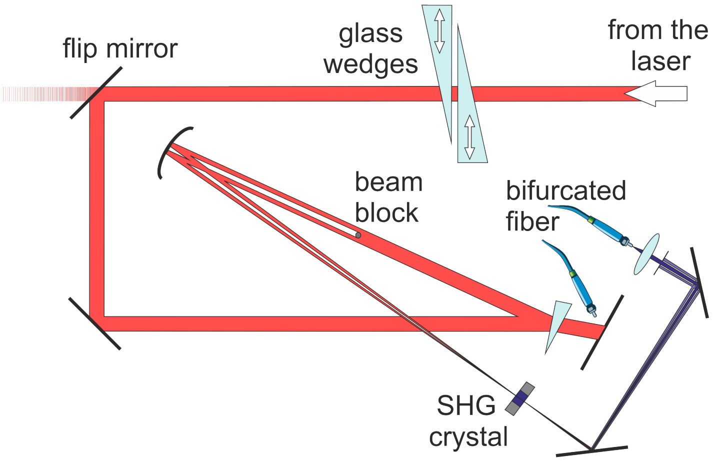

Figure 3.2.: Sketch of the D-Scan setup. After the chirped-mirror compressor, the laser pulses pass through the glass wedges for dispersion fine-tuning. By means of a flip-mirror mount, the beam is coupled into the D-Scan setup. The front reflex of a small wedged window is split by a beam block and used to generate the SHG signal in non-collinear geometry in the BBO crystal. Solely the SHG signal passes the filter and is coupled into one arm of a bifurcated fibre, whereas the other arm picks up the diffuse reflex of the fundamental, which passed the wedged window.

shutters were built from simple servo motors which are controlled by an Arduino Leonardo microcontroller which in return gets commands from a Labview program on a standard PC.

3.2.1. Wedge Alignment

In order for the D-Scan to work, the wedge insertion into the beampath has to cover some millimeters (~ 3 mm) of glass dynamic range. The wedges are carefully aligned to have the surfaces facing each other perfectly parallel—else would result in a pulse-front tilt. Experimentally, an orientation angle of the wedges with respect to the incident laser beam was found, which minimizes the beam displacement behind the wedges upon moving them. This was found desirable to reduce influences on any setup behind the wedges. As a unique feature, this angle was further exploited for the calibration of the amount of glass inserted into the beam path. To determine this angle, a ray-tracing script written with Matlab[35] was used. The resulting angle of incidence on the first wedge was found to be 28.16°. When the wedges move, the beam path changes and the change in path length which the beam spends in the glass corresponds to the effective amount of glass insertion. With the ray-tracing script the glass insertion was determined to be 13.81 % of the relative displacement of the stages. The influence of dispersion within the wedges on the beam path was found to be negligible. The only assumption made in the computation is that the laser beam propagates parallel to the optical table.

3.3. Phase Retrieval

The phase retrieval algorithm takes a measured D-Scan trace $S_{meas}(\omega, z)$ and fits a theoretical trace $S_{sim}(\omega, z)$ simulated according to equation 3.1 to it. To this end, it computes the spectral electric field from the measured fundamental spectrum and varying spectral phases. Then it evaluates which phase function is suited best to have good agreement with the measurement. The iterative algorithm chosen to compute the fit is the Nelder Mead or Downhill Simplex algorithm[39; 14], which is a versatile tool to solve multidimensional optimization problems and is explained in detail in section 3.4. Here, it is used to minimize the error function G, which is defined as the integrated, least-square difference between the measured trace $S_{meas}(\omega, z)$ and a simulated trace $S_{sim}(\omega, z)$:

$$G = \sqrt{\frac{1}{N_i N_j} \sum_{i,j} \big(S_{meas}(\omega_i, z_j) - \mu S_{sim}(\omega_i, z_j)\big)^2}. \tag{3.2}$$

For numerical evaluation the traces are discretized to functions of the discrete variables ω_i and z_j, which are arrays of length N_i and N_j respectively. μ is a scaling factor, which minimizes the error in each iteration. Because here it fulfills the additional, important function of a spectral-response filter, it will be discussed in detail in section 3.3.1.

As mentioned above, the spectral phase, which the D-Scan tries to retrieve, is varied systematically according to the results of the error function G. For this reason, it is not possible to start off with an analytic expression for the spectral phase, which would restrict its variation. In fact, in the implementation of the D-Scan, the phase is rather given through a set of evenly spaced supports in the spectral domain, which can be fed into the Downhill Simplex algorithm.

Because prior knowledge about the algorithm is helpfull to understand the exact construction of the spectral phases used in the iteration, further explainations are postponed to section 3.4.1.

With this in mind, the basic steps of the retrieval algorithm are:

(i) Start with an initialized/random phase function $\varphi(\omega)$.

(ii) Simulate a D-Scan trace according to equation 3.1.

(iii) Compute the error function G.

(iv) Based on the value returned, choose a better phase function.

The last step is left to the automated Downhill Simplex algorithm (see section 3.4) and steps (ii)-(iv) are repeated until the error converges.

3.3.1. Spectral Response

When fitting the simulated trace $S_{sim}(\omega, z)$ to the experimental data, the goal is to reproduce the shape of $S_{meas}(\omega, z)$. However, even if the two traces match, but are not scaled with repect to each other, because the expression for $S_{sim}(\omega, z)$ is only defined up to a constant, the error G is artificially increased. This is the first reason to introduce the scaling factor μ in equation 3.2. Considering the error function as a linear least squares problem, μ would be the overall factor that minimizes the error G in order to ensure a good fit. It has to be updated for each iteration of the algorithm and can be derived by evaluating the derivative of G with respect to μ:

$$\frac{\partial G}{\partial \mu} \overset{!}{=} 0. \tag{3.3}$$

As mentioned before, the second reason to have a scaling factor in the error function is that it may be used to mimick a spectral response filter. Without the consideration of an inhomogeneous spectral response, the measured trace is assumed to behave as perfect as equation 3.1 predicts, which is unrealistic. For example neither the SHG conversion efficiency, nor the transmission of the optical fibres, which couple into the spectrometer, can be expected to be the same for all frequencies. These effects become even more pronounced, as the second harmonic of a Ti:sapphire laser can be expected in the range between

300-500 nm, which on the one hand is close to the edge of the transparency window of most glasses and on the other hand quite a large bandwidth for the SHG process to cover. While measuring or estimating these spectral properties is not done easily, here they are included in the minimization of the error function G. By making the scaling factor frequency-dependent $\mu \to \mu_i = \mu(\omega_i)$, it tries to minimize the error between $S_{meas}(\omega, z)$ and $S_{sim}(\omega, z)$ for every frequency independently. If *e.g.* high frequency components in the measured signal, were absorbed in the fibres, but are visible in the simulated trace, μ_i rescales the simulated trace in this spectral region. Note that this does not affect the shape or landscape features to be fitted, as their information is also encoded in the amount of glass insertion. What is more, the spectral response of the overall system is retrieved as a side-product at the end of the iterative algorithm as the frequency-dependent scaling factor μ_i.

Finally, replacing μ by μ_i in the error function and evaluating the derivative of G with respect to μ_i as in equation 3.3, the following expression for μ_i can be found:

$$\mu_i = \frac{\sum_j S_{meas}(\omega_i, z_j) S_{sim}(\omega_i, z_j)}{\sum_j S_{sim}(\omega_i, z_j)^2}. \tag{3.4}$$

3.4. The Downhill Simplex Algorithm

The Downhill Simplex algorithm searches for extrema based on a systematically proceeding, heuristic method. It has the advantage over gradient-based methods of not using any derivatives of the function it minimizes, which may—as for the error function G in the case of the D-Scan—be complicated. A simplified version of the textbook illustration of the algorithm by Geiger and Kanzow [15] will be sketched here.

The goal of the algorithm is to find the minimum of a function $f : \mathbb{R}^n \to \mathbb{R}$, which takes n input variables and returns one output value, where n will be called the dimension. Now we take $n + 1$ sets of these n input variables $x^1, \dots, x^{n+1}$. Any of these mutually different sets of parameters $x^i \in \mathbb{R}^n$ is a vertex of an n dimensional object we call a simplex as illustrated in figure **??** for the case $n = 2$. By evaluating the function f at each vertex of the simplex, they can be ordered with respect to the functions output:

$$f(x^b) \leq \cdots \leq f(x^w). \tag{3.5}$$

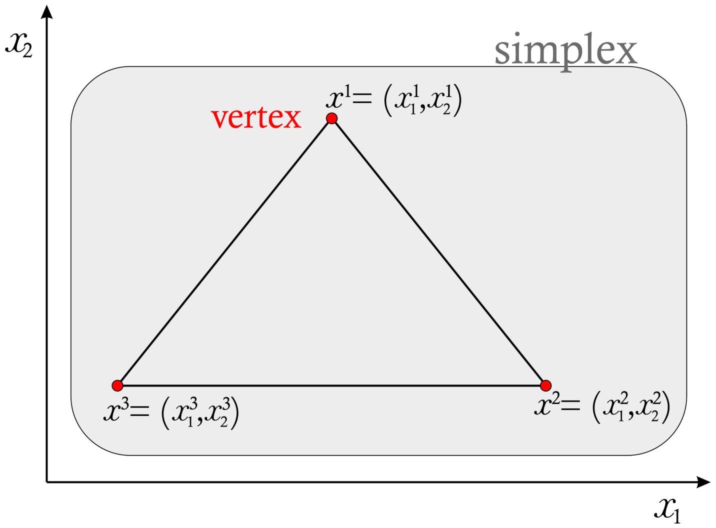

Figure 3.3.: In $n = 2$ dimensions a simplex has $n + 1 = 3$ vertices, which can be depicted as the coordinates of the corners of a triangle. In three dimensions, the simplex is an irregular tetrahederon, whose four corners/vertices are described by the three spatial dimensions. In higher dimensions, the simplex is a rather unituitive hyper-cube.

Here, x^b and x^w denote the best/ worst vertex, respectively, which means at any point during the iteration, x^b is the best approximation to the minimum of f, while x^w is the worst.

Now the algorithm tries to construct a better simplex based on the n best vertices of the old one. The single steps are drawn out in the following pseudo code:

Choose parameters $\alpha > 0$, $\beta > 1$ and $0 < \gamma < 1$ and an initial simplex with vertices $x^1, \ldots, x^{n+1} \in \mathbb{R}^n$.

For each iteration step:

Determine x^b, x^w and the centeroid of the n best vertices $\overline{x} = \frac{1}{n} \sum_{i=1; i \neq w}^{n+1} x^i$.

- **Reflection:** Compute x^r by reflecting the worst vertex on $\overline{x}$:

$$x^r = \overline{x} + \alpha(\overline{x} - x^w),$$

and evaluate $f(x^r)$. If $f(x^b) \leq f(x^r) \leq f(x^w)$, replace x^w with x^r.

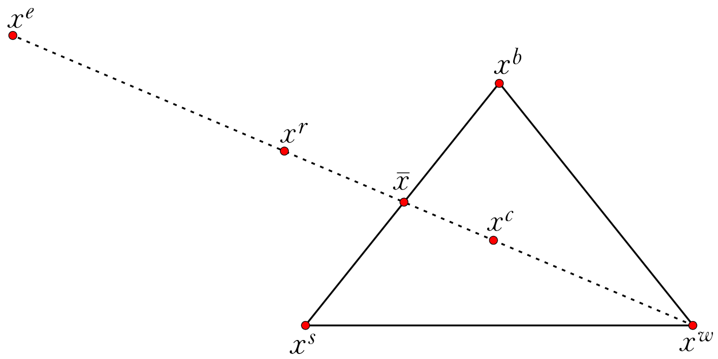

Figure 3.4.: In each iteration of the algorithm, the existing vertices are evaluated in order to construct a new vertex. Calculating $\overline{x}$ from the best and second best vertices x^b and x^s, the worst vertex x^w is then reflected/ expanded/ contracted along the dashed line.

- **Expansion:** If $f(x^r) < f(x^b)$, compute the expansion vertex x^e:
  $$x^e = \overline{x} + \beta(x^r - \overline{x}).$$
  Evaluate $f(x^e)$ and replace x^w by x^e.
- **Contraction:** ElseIf $f(x^r) > f(x^w)$, compute the contraction vertex x^c:
  $$x^c = \overline{x} - \gamma(x^r - \overline{x}).$$
  Evaluate $f(x^c)$ and replace x^w by x^c.

Repeat, until the simplex fulfills the convergence criterion.
The different steps are illustrated for the two dimensional case in figure 3.4 and can generally be interpreted as follows. Using the reflection alone, if $f(x^b) \leq f(x^r) \leq f(x^w)$, each new simplex is an improvement to the previous. But if the reflection vertex is already better than the best vertex, the hope that there may be more to gain in this direction is justified and an expansion is executed. The other possibility—the new vertex is worse than any other—is caught by contracting the new vertex into the simplex center.

The algorithm was implemented as described above in the graphical programming language Labview and tested to work satisfactorily. Although different implementations of the single decision steps are possible, the one proposed here is simplified compared to examples in published literature. Nevertheless, it seems to suffice, as a more elaborated version following [14] and [15] did not converge any better. Furthermore, a shrinking step excluded here, always let the algorithm run into a dead end. The shrinking step is designed to follow up on contractions, in case any newly generated vertex is worse than x^w. An assumption is that in high dimensions—where the risk to converge into local minima is substantial—this step runs the risk to shrink the simplex too drastically, such that it gets easily stuck afterwards.

The reflection, expansion and contraction parameters (α, β, γ) were choosen according to Gao and Han [14], who claim their set works better in higher dimensions, than the standard set $(1, 1/2, 2)$. Neither could this claim be confirmed, nor be proven wrong. The expressions for the parameters are:

$$\alpha = 1, \quad \beta = 1 + \frac{2}{n}, \quad \gamma = 0.75 - \frac{1}{2n}. \tag{3.6}$$

3.4.1. Phase Construction

Now that we have established the Downhill Simplex algorithm as a minimization technique, we can clarify how it is used to find the phase, which minimizes the error function G.

In general, any set of basis functions e.g. sines & cosines, polynomials, *etc.* could be used for this purpose. Here, an approach based on spline interpolation, which proved very flexible, was implemented. It directly translates each of the $(n+1)$ n-dimensional vertices of a simplex to a one dimensional phase function. The most direct way to do so, which is also illustrated in figure 3.5, is to employ the values of the vertices directly as phase amplitudes at an automatically generated set of hinges, which are thereafter linked by interpolated splines. The splines used here are 2^{nd} order polynomials. Two other, similar methods to build a phase function, were implemented as well. There, the vertices are translated to functions of the group delay and group delay dispersion (see sec. 2.1.2) in the same manner as described above and are then integrated numerically once or twice respectively, in order to yield a phase function. Essentially, all of these descriptions are equivalent, as constant and linear phases—which remain ambiguous in the integration—do not alter the D-Scan traces. Actually, it can be shown analytically that constant and linear phase terms cancel out of equation 3.1. For this calculation, the reader is referred to appendix A.1.

The usage of splines as a basis set has the inherent benefit that the effort to reconstruct a simplex from a given phase function—the inverse process of the

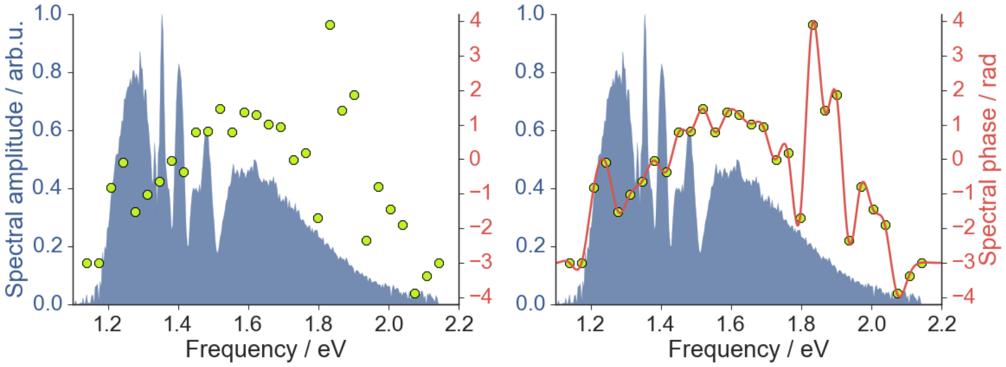

Figure 3.5.: A phase function is build from the vertex of a simplex: In the spectral region where the spectral amplitude (blue) is non-zero, an evenly spaced array with the same length as a vertex is set up. (Left) The single vertex values (green) now translate to the amplitudes of the phase at these positions. (Right) In a second step, a smooth phase function (red) is interpolated from these discrete supports using spline interpolation.

phase construction described above—is low. To do so, the phase function or its derivatives are sampled by an evenly spaced array and the amplitudes at these positions, which basically represent one vertex, are used for the initialization of a new simplex. This facilitated to implement the following features in the algorithm:

- **Save & Load:** A phase function retrieved from the algorithm can be stored. If there is good reason to assume that this phase might be a good starting point for another retrieval it can be loaded and converted to a simplex, in order to speed up convergence.

- **Finer/Coarser Sampling:** When a retrieval with a different sampling compared to a prior analysis is desired, the latter can be used, instead of starting out from zero. To this end, the phase function from the previous or a saved retrieval is resampled at the desired number of sampling points and taken into account during initialization of the new run.

It must be mentioned that recreating a phase function by sampling it and rebuilding it with splines is not perfect, in a sense that the new phase is not an exact copy of the old. But the difference is small enough to be neglected in practice, as the algorithm introduces new variations to the phase upon reinitialization anyway.

3.4.2. Convergence Criterion

Because the Downhill Simplex algorithm—and with it the whole phase retrieval—is an iterative procedure, the convergence towards the *true* phase function has to be discussed. Within this scope, the number of parameters, which sample the phase and the maximum number of iterations allowed, have to be considered as well. Here, these topics are addressed, prior to the systematic analysis of the algorithm in section 3.5.

From the different approaches in literature to define a convergence criterion for the Downhill Simplex algorithm, the one originally proposed by Nelder and Mead [39] was implemented. It relies on the standard deviation of the function evaluations $f(x^i)$ of all the vertices x^i of the simplex:

$$\sqrt{\frac{1}{n}\sum_{i=1}^{n}\left(f(x^i)-\overline{f}\right)^2} < \epsilon, \tag{3.7}$$

where $\epsilon > 0$ is a constant and $\overline{f} = \frac{1}{n}\sum_{i=1}^{n} f(x^i)$ is the mean of the function evaluations. As this convergence criterion describes the spread of the function evaluations, it is a good measure for the potential to improve with further iterations. If the function evaluations clump together, all vertices of the simplex are just about equally far away from the target, which makes the decision-making of the algorithm harder, but does not necessarily lead to much more improvement. Thus, depending on the quality of the data, ϵ is set to a value between 0.05 and 1 to stop the iteration, when the standard deviation of the function evaluations is below this threshold.

As convergence is not at all guaranteed, an upper limit to the number of iterations is used to stop the algorithm as a contingency plan. With the algorithm fully parallelized, ~180 iterations/s are possible on a standard computer, which allows to do a retrieval with 30 000 iterations in less than 3 min.

For practical reasons—mainly the runtime—the size of the vertices has to be restricted to a reasonable value. On the one hand, more parameters within a vertex can be beneficial, because the sampling of the phase has to be fine enough to retrieve its details. On the other hand, for large, n-dimensional vertices, a simplex contains $(n + 1)$ of these, which all have to be initialized and then updated one after the other. So not only is the computational cost higher, because the arrays to be handled are larger, but it takes longer until each individual vertex has been updated, because of the sequential nature of the

Downhill Simplex algorithm. To find a good tradeoff between the dimension of the vertices and the number of iterations needed, these parameters are evaluated in section 3.5.

3.4.3. Initialization

Before the Downhill Simplex algorithm can start the minimization, an initial simplex has to be generated [3]. As a starting point, this simplex should be made up of vertices, which represent spectral phase functions that are mutually different in order to offer the algorithm a good choice to start the contraction of the simplex, but that should still in some sense be reasonable as to not blow up the simplex too much, which lengthens the retrieval.

As a first approach to introduce phase variations all over the spectral range covered by the spectral amplitude, every vertex of the simplex is initialized such that it is translated to a narrowly peaked phase function each with a different center frequency. This method is illustrated in figure 3.6. Depending on the number of vertices in the simplex, the shape of the dips changes slightly. As more dips effectively cover the same range, they become narrower. This way of initializing the simplex was used many times and never failed to converge sooner or later.

A second method, which initializes the whole simplex with random numbers from the open interval $(-1, 1)$ was implemented as well. Here, the problem arises that the initialization is sometimes not successfull, when the vertices are initialized as a function of the group delay or group-delay dispersion. Through the integration of these functions to the phase domain, the Downhill Simplex algorithm apparently can get stuck, when the initial simplex is too far off or too large. Thus, it is recomended to use this initialization only under supervision. When the initial phase functions are build directly from splines between hinges with random amplitude, the algorithm is more successful. In the evaluation, this approach was compared to the one described above and found to be inferior.

In order to test the dependency of the algorithm's outcome on the method of initailization, a third scheme, which is a combination of the ones described above, was tested as well. Here, the dips from the first method are scaled by a random factor from the interval $(0.3, 1.3)$ and negated with a chance of 50 %. The results of this initialization scheme comply with the ones from the first

---

[3] Recall the pseudo code in section 3.4.

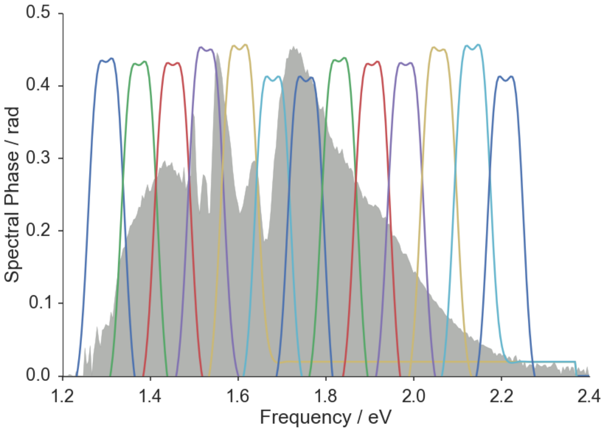

Figure 3.6.: Each vertex is initialized as an individual dip along the spectral range covered by the spectral amplitude. Here, only every third of a total 40 vertices is shown, else the figure would be too crowded.

scheme, but the algorithm takes longer to reach convergence. Surely, this does not prove the independence of the results of the algorithm on the method of initialization since the two schemes compared are alike, but it suggests that there is no trivial dependence.

3.5. Evaluation

The three main factors, which determine the performance of the retrieval algorithm are the number of parameters from which the phase functions are built, the maximum number of iterations the algorithm may perform and the noise level of the measurement data. The results of different evaluation programs, in which these parameters were varied systematically, are presented here. For each set of input parameters, the phase retrieval was performed ten times and the results of these runs were averaged. Two measures of the retrieval quality are shown in the following sections: (1) The averaged retrieved spectral phase and the associated standard deviation and (2) the mean FWHM of the pulses, which were obtained by Fourier transformation of the spectral field.

Since the true spectral phase of the pulses cannot be accessed without another characterization device, there are two methods to validate the retrieval algorithm. First, we can check, how well consecutive retrievals from the same measurement data match. If it is not consistent by itself, there is little reason to trust any of its results. This aspect of the evaluation is covered in section 3.5.1. The second instrument at hand is to simulate D-Scan measurements with an constructed phase function in order to try to retrieve it. Artificial noise can be added to the simulated measurements to mimick the real data. This kind of accuracy check is addressed in section 3.5.2.

3.5.1. Consistency Check

In order to test the consistency of several retrievals of the D-Scan algorithm, the results of ten runs of the algorithm—the spectral phase and the FWHM of the temporal pulses—were averaged. This procedure was repeated for different settings, which consisted of taking a number from the set $[50, 70, 90, 110, 130]$ as the number of parameters which provide the hinges for the spectral phase and limiting the maximal number of iterations of the algorithm to a value in the set $[18000, 30000, 42000]$. The resulting phases for two sets of data are shown in figures 3.7 and 3.8 and the corresponding FWHM's are plotted in figure 3.9.

In the figures 3.7 and 3.8 it can be observed that the standard deviation for lower parameter numbers is considerably higher, which indicates that a certain number of parameters is necessary to obtain a good retrieval. A possible explanation of this effect is that the details of the phase cannot be resolved with too few parameters because the anchor points do not sample the spectral domain fine enough. Thus, instead of finding a minimum, the algorithm does not converge to the *true* phase and consequently will not do it either upon the next retrieval.

The lower left plot in figure 3.7, where a large number of parameters and few iterations were used for the retrieval, shows huge deviations from the mean. Because $(n+1)$ vertices for n parameters are needed it takes much longer until all vertices of a simplex are updated when n is large. Thus, 18 000 iterations were simply not enough in this case to come close to convergence.

As a result from the observations above, it is suggested to use at least 90 parameters in order to resolve the details of the phase, but not more than 110, because it would slow down the algorithm. It should also be mentioned that the Downhill Simplex algorithm becomes increasingly inefficient in high dimensions[14], which is an additional reason why the number of parameters should be kept as low as possible.

Figure 3.9 shows the FWHM calculated from the retrieved spectral phases and the corresponding spectral amplitudes. The values for few iterations (blue) differ from the results with more iteration steps (green, red) and fewer parameter numbers seem to overestimate the FWHM. The error bars of the individual points as well as the standard deviation of all points around their mean (solid lines) suggest that a first estimate of the D-Scan's accuracy is ~ 0.1 fs. While the topic of the accuracy of the algorithm will be addressed in the next section, these plots show the consistency of the retrieval is quite good provided that enough parameters and iterations are used.

In all the D-Scan measurements, which were recorded while the laser system described in section 2.3 was active, a trace consisted of 100 spectra taken at different amounts of glass insertion. In retrospect, it was found that 50 spectra with a coarser sampling of the glass insertion yield the same results, while their computation takes only half as long. The plots that support this claim and which correspond to the same data sets as the plots shown here, may be found in appendix A.2.1.

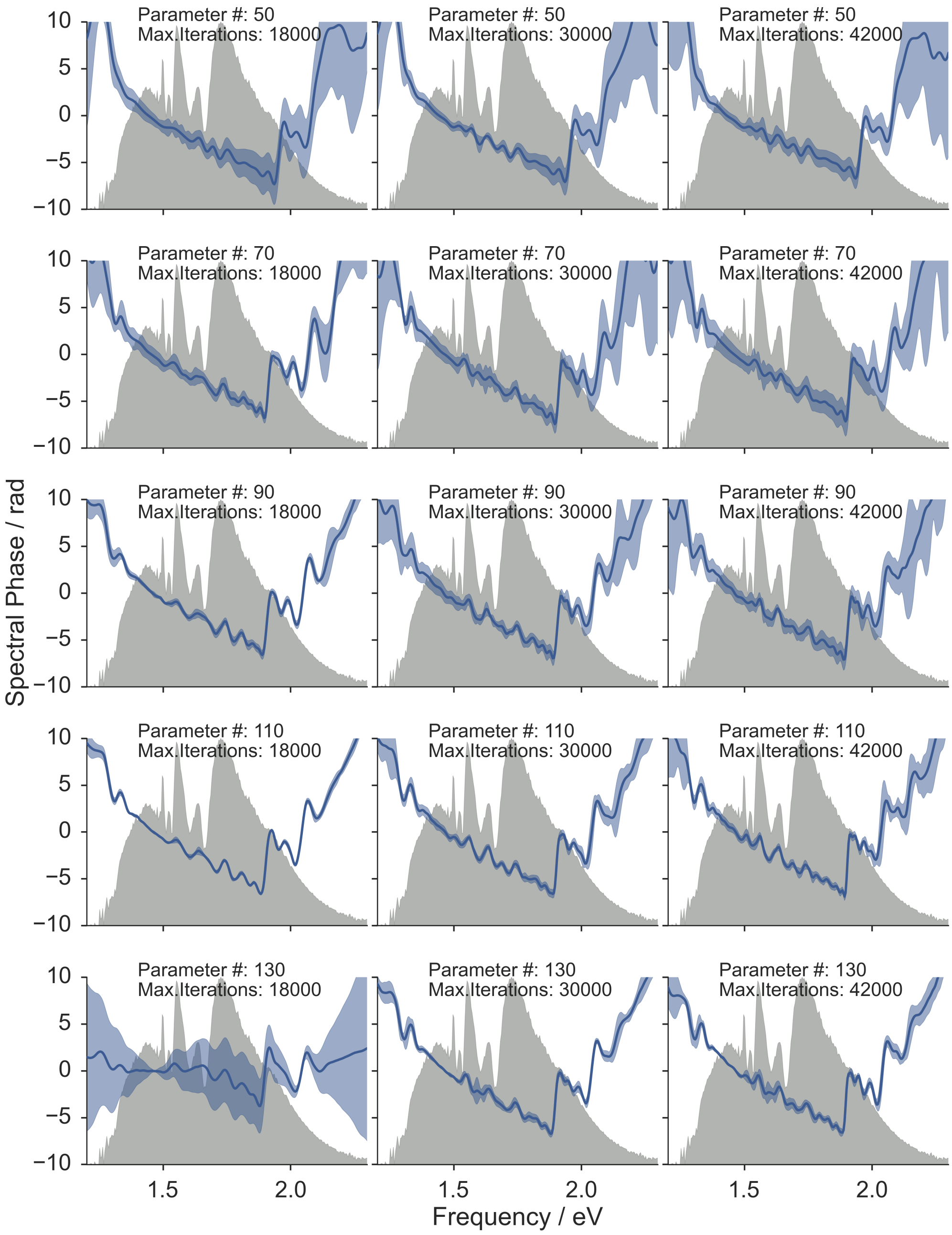

Figure 3.7.: Mean spectral phase (blue) and its standard deviation (light blue) from ten consecutive retrievals of the same data set with different boundary conditions. The number of parameters that build the phase is increased from top to bottom. The number of iterations is increased from left to right. The spectral amplitude (grey) is shown in the background.

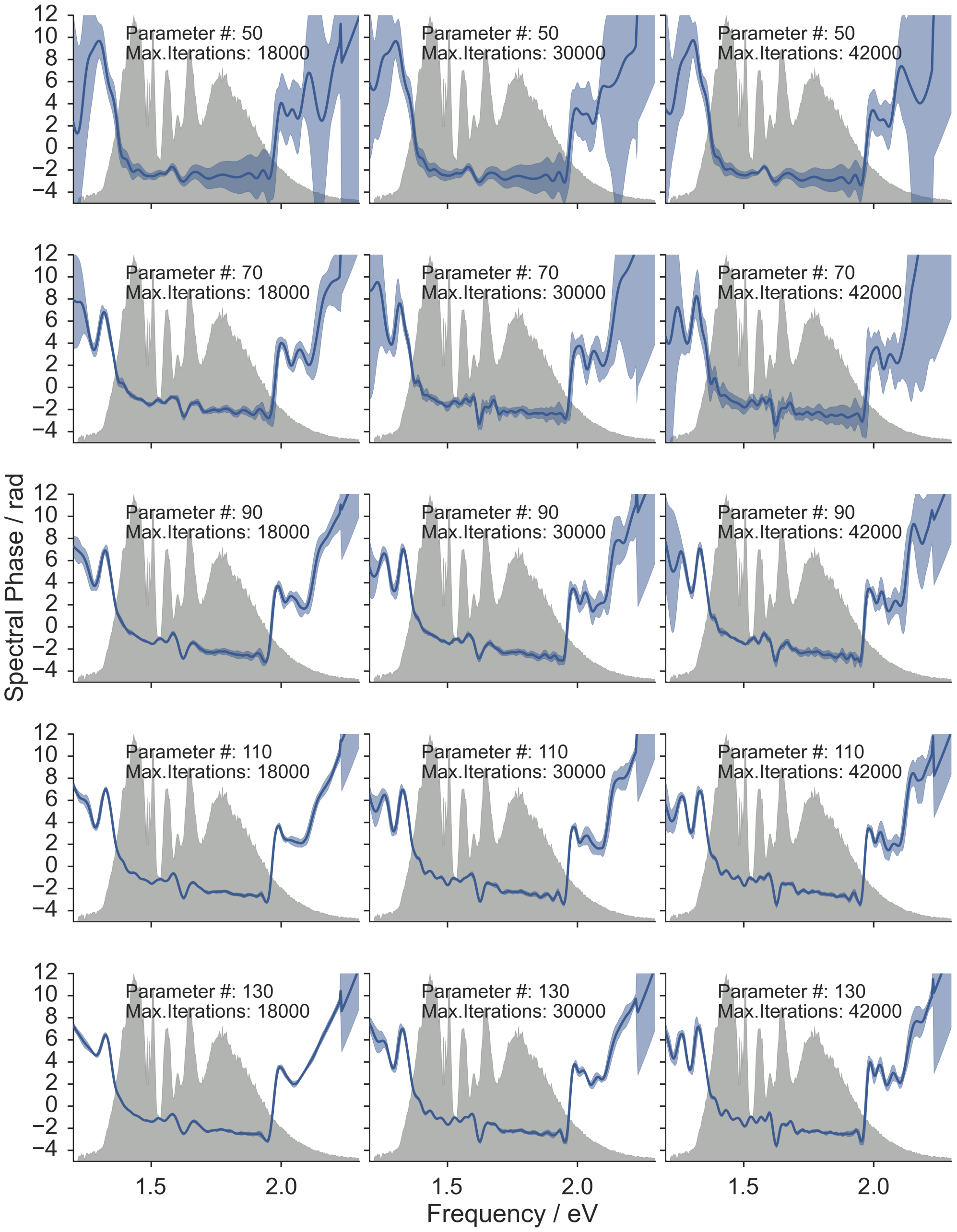

Figure 3.8.: Mean spectral phase (blue) and its standard deviation (light blue) from ten consecutive retrievals of the same data set with different boundary conditions. The number of parameters that build the phase is increased from top to bottom. The number of iterations is increased from left to right. The spectral amplitude (grey) is shown in the background.

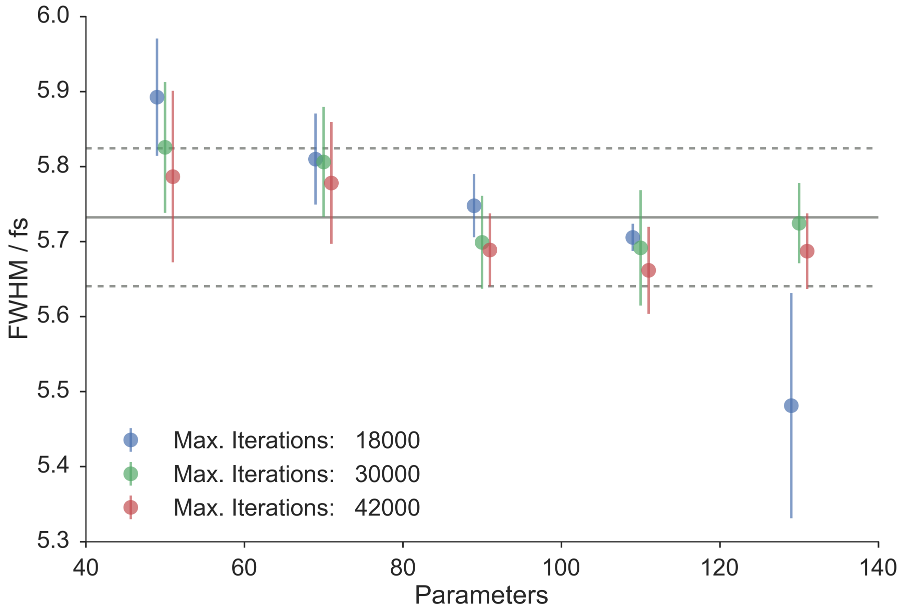

(a) FWHM data corresponding to figure 3.7.

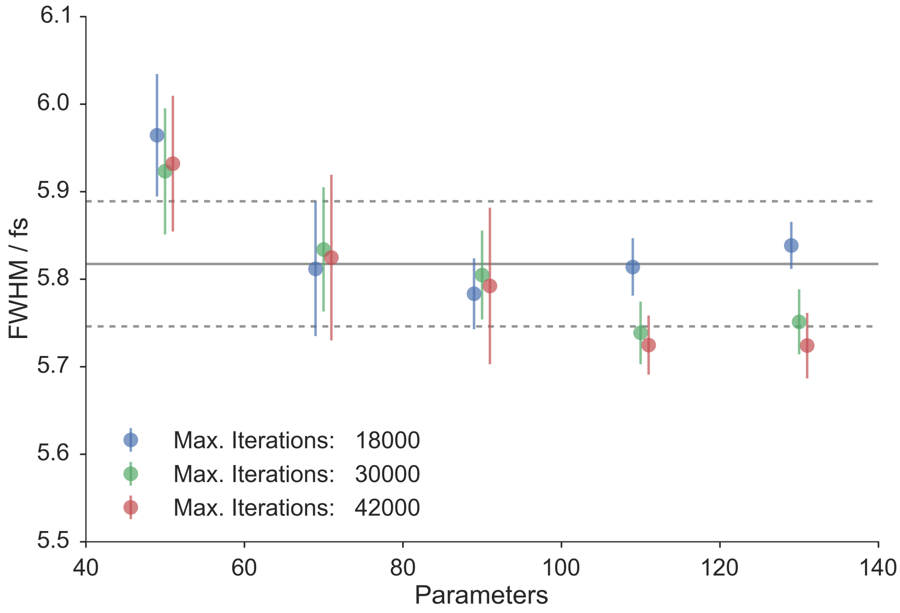

(b) FWHM data corresponding to figure 3.8.

Figure 3.9.: Full width at half maximum of the pulses which are obtained from the spectral phases and amplitudes in the previous plots as a function of the number of parameters that built the phase functions and the number of iterations of the algorithm. The average of all values is indicated by the solid line with a confidence interval of one standard deviation (dashed lines).

3.5.2. Accuracy Tests

To estimate the accuracy of the algorithm, simulations of D-Scan traces were calculated and subsequently the phases were retrieved under different conditions.

In order to test the behaviour of the algorithm towards noisy signals, retrievals from simulated traces with added Gaussian noise were performed. The standard deviation of the noise distribution was set to 0 %, 3 %, 6 %, 9 %, 12 % and 15 % of the maximum of the second-harmonic signal trace. The number of parameters was varied as well, while the number of iterations was fixed at 30 000. The results of the retrieval of two exemplary phase functions are displayed in figures 3.10 and 3.11 while figure 3.12 shows the corresponding FWHM values as a function of the noise amplitude. Figure 3.13 shows the retrieval under the same conditions as for figure 3.11, but initialized with the random scheme described in section 3.4.3. It is evident that this scheme is less successful to ensure a good phase retrieval and would need more iterations to reach a satisfactory approximation of the input phase.

As expected, the plots demonstrate that the phase retrieval is worse the higher the noise is. Yet even for high noise levels, the retrievals are quite successful. Further, the uncertainty is higher at the wings of the spectrum. This is due to the non-linearity used to generate the D-Scan trace. Wherever the spectral amplitude is low, the SHG efficiency drops dramatically, which makes the phase retrieval in these spectral regions more difficult. In the center of the spectrum of the pulses the phase is recovered well even for high noise levels. As for the number of parameters used in the retrievals, the results show no tendency to become better with increasing parameter numbers.

An interesting feature in figure 3.11 is that the retrieval introduces a phase jump in the high frequency wing of the spectrum in most cases. After the sudden jump, the rest of the phase is retrieved correctly in most cases. Since the same phase step is retrieved in many times and because it has a height of about 2π, it is assumed to leave no trace in the simulation of the D-Scan traces and to be a systematic error of the algorithm. It should not affect the FWHM of the pulses, since a constant phase jump of 2π in the spectral phase cancels analytically. In the retrievals of the measurement data presented in section 3.6, more of these jumps appear. An assumption is that the initialisation method is responsible for this behaviour of the algorithm.

From figure 3.12 we see that the FWHM of the pulses is recovered well by the algorithm. For moderate noise levels, the values from the retrieval fall with high certainty within an interval of less than ± 0.2 fs of the input value. In accordance with the error discussed at the end of the last section, the value of ± 0.2 fs is proposed to be taken as a conservative estimate of the general error of the D-Scan characterizations.

To determine after how many iterations the algorithm can be expected to have reached convergence, a set of simulations with different upper limits to the number of iterations was executed. Figures 3.14 and 3.15 show how an increased number of iterations results in a better retrieval of the spectral phase. The effect is more pronounced for the more complicated phase function shown in figure 3.15. Furthermore, it can once more be observed that high parameter numbers are necessary in order to retrieve the fine details of the phase. As can be seen from figure 3.16, the FWHM are not quite as sensible to the number of iterations. An acceptable deviation from the goal value is already reached after 20 000 iterations.

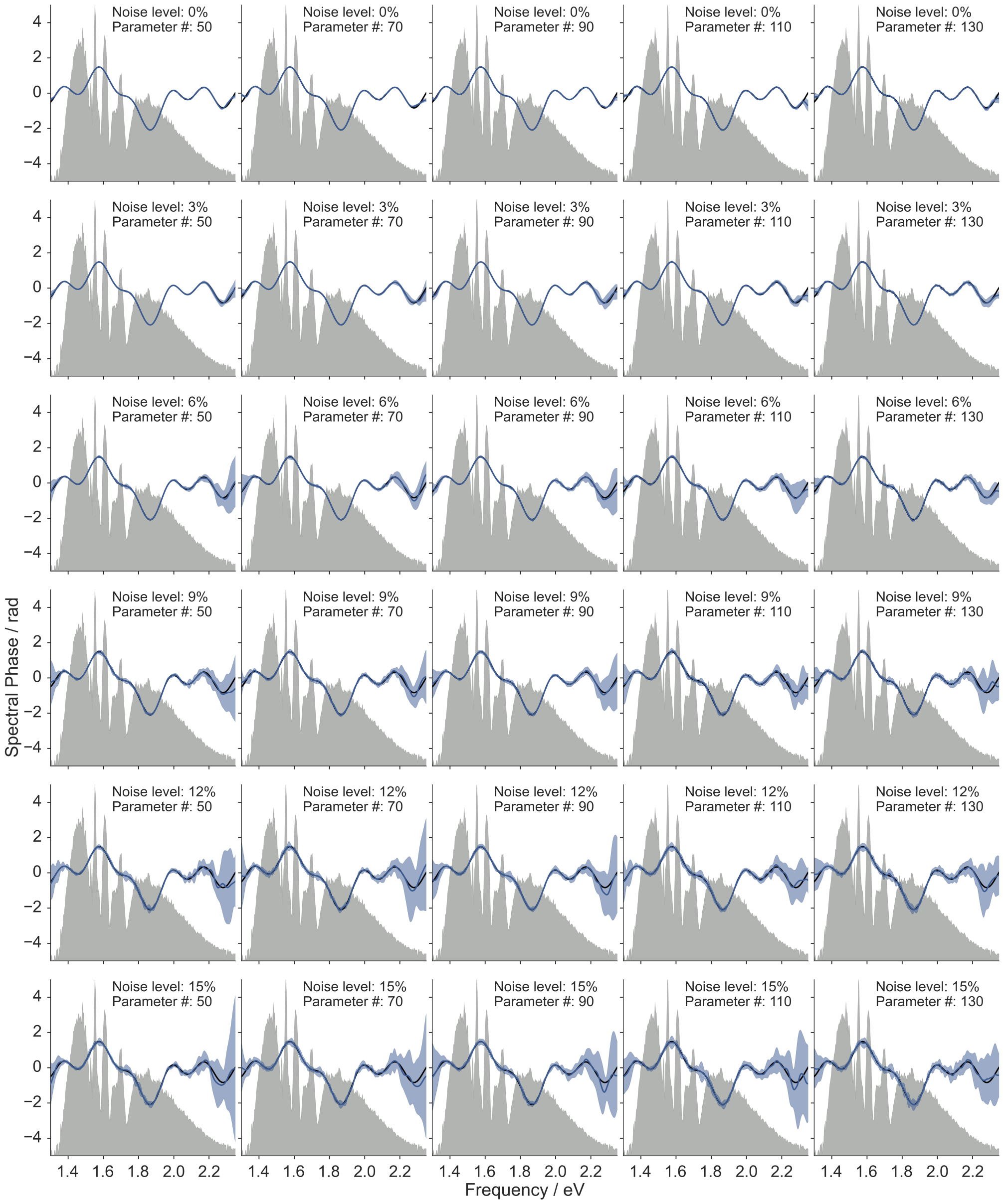

Figure 3.10.: Mean spectral phase (blue) and its standard deviation (light blue) from ten consecutive retrievals performed on simulated data. The input phase is plotted in black and is almost entirely covered by the retrieved phase in most plots. The noise on the simulated data increases from top to bottom. The number of parameters in the retrieval is increased from left to right. In the background the spectral amplitude (grey) is shown.

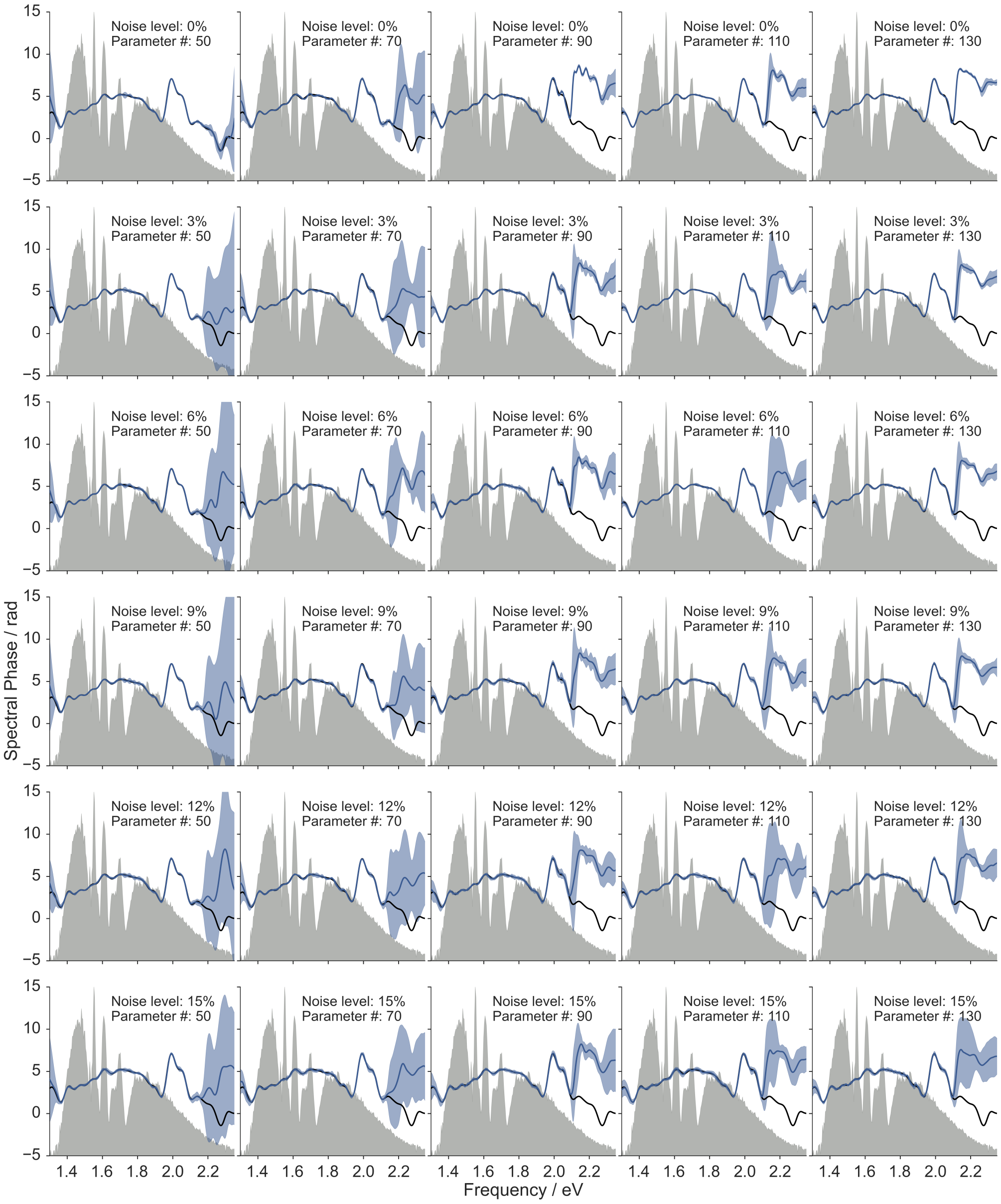

Figure 3.11.: Mean spectral phase (blue) and its standard deviation (light blue) from ten consecutive retrievals performed on simulated data. The input phase is plotted in black. The noise on the simulated data increases from top to bottom. The number of parameters in the retrieval is increased from left to right. In the background the spectral amplitude (grey) is shown.

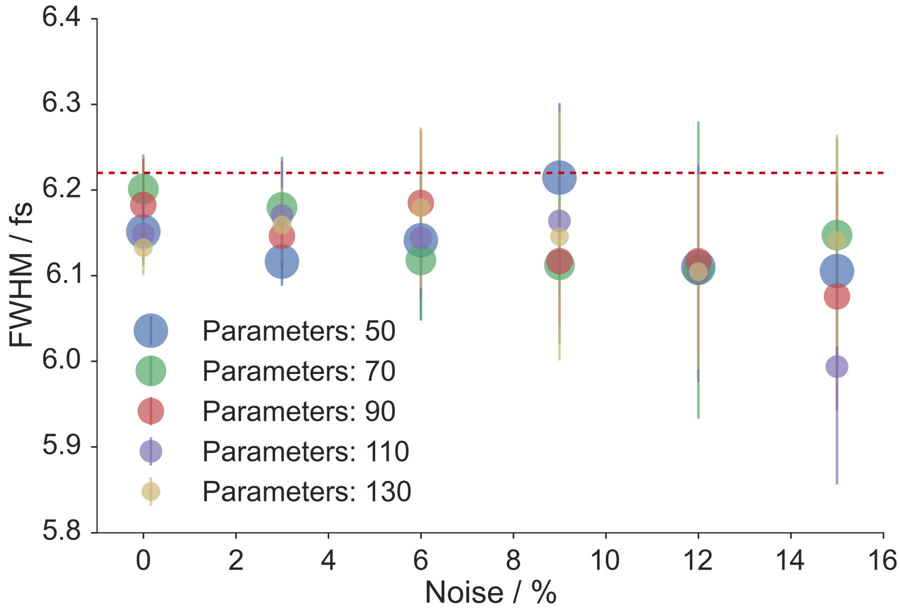

(a) FWHM data corresponding to figure 3.10.

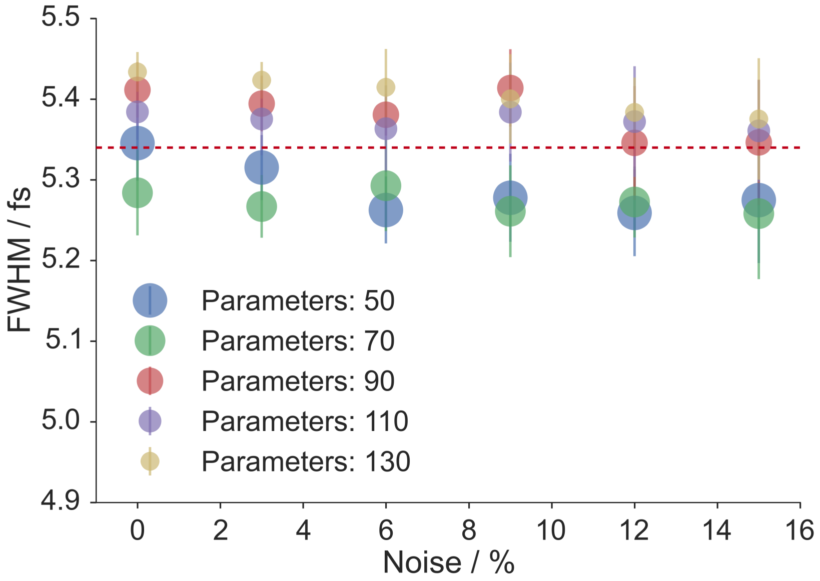

(b) FWHM data corresponding to figure 3.11.

Figure 3.12.: Full width at half maximum of the pulses which are obtained from the spectral phases and amplitudes in the previous plots as a function of the number of parameters that built the phase functions and the amplitude of the noise added to the traces. The values which correspond to the input phases of the simulations are indicated by the red dashed lines.

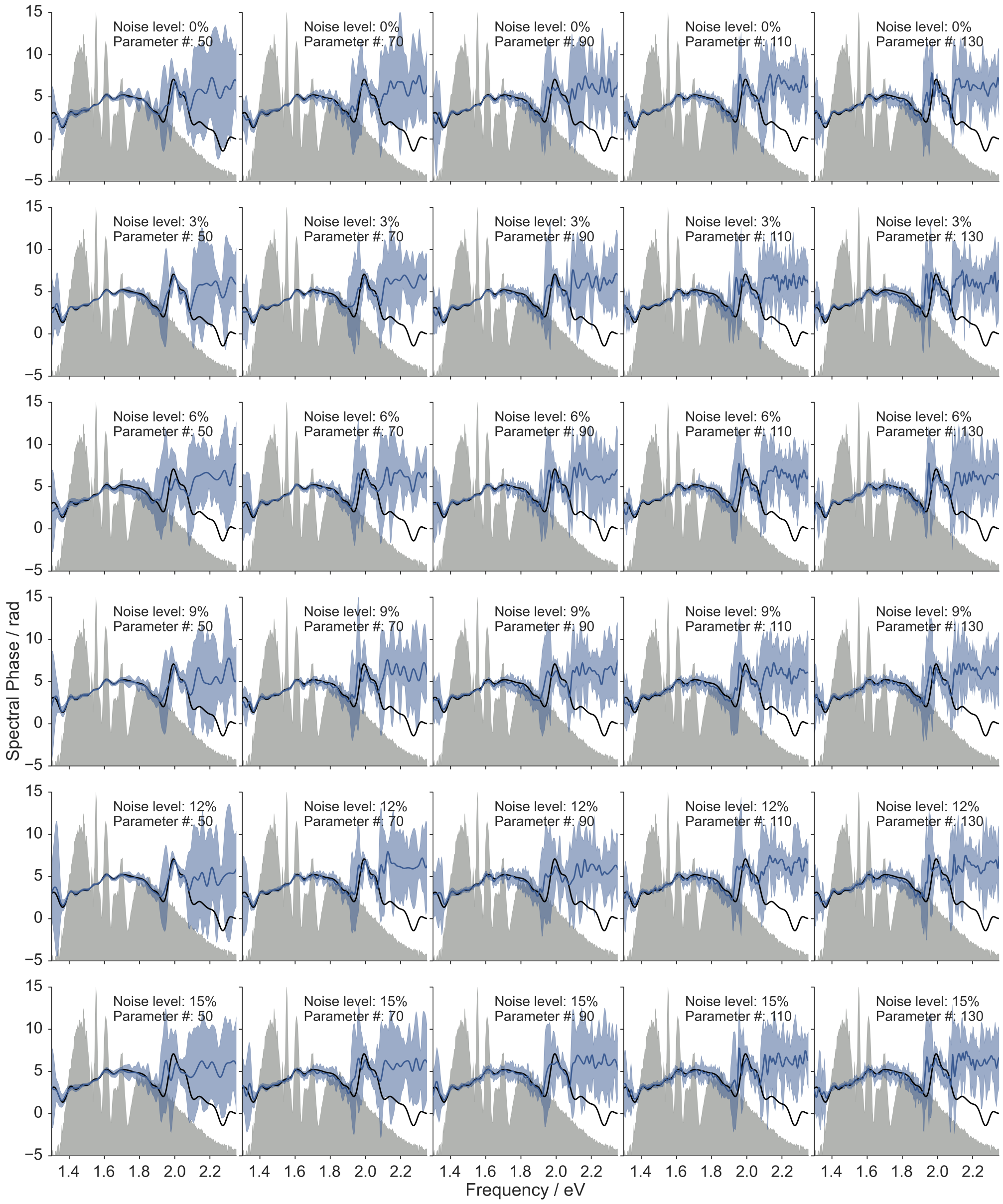

Figure 3.13.: Mean spectral phase (blue) and its standard deviation (light blue) from ten consecutive retrievals with random initialization performed on simulated data. The input phase is plotted in black. The noise on the simulated data increases from top to bottom. The number of parameters in the retrieval is increased from left to right. In the background the spectral amplitude (grey) is shown.

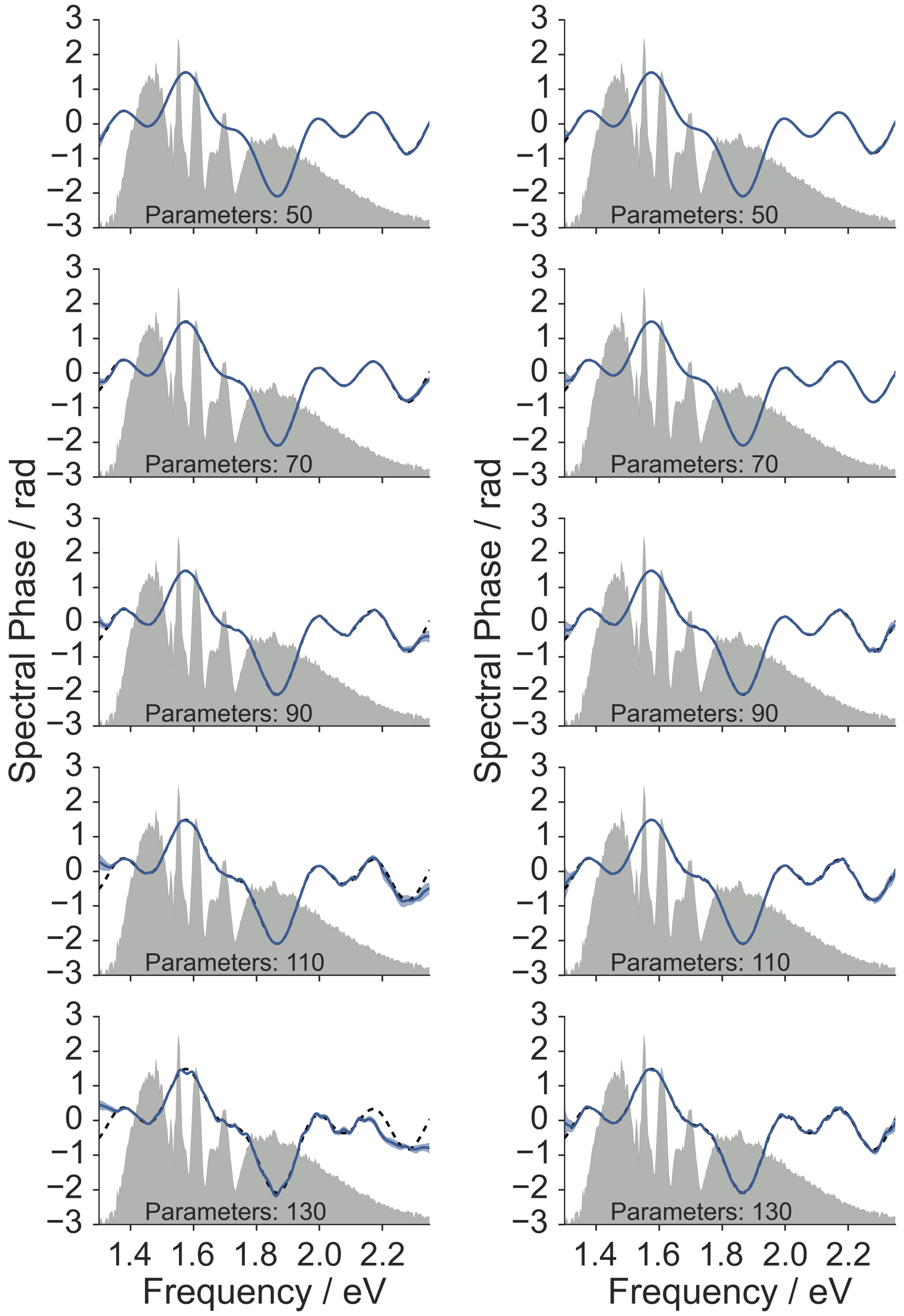

(a) Retrievals with 10 000 iterations. **(b)** Retrievals with 30 000 iterations.

Figure 3.14.: Mean spectral phase (blue) and its standard deviation (light blue) from ten consecutive retrievals performed on simulated data. The input phase, which is the same as in figure 3.10, indicated by the black dashed line. The number of parameters in the retrieval is increased from top to bottom. In the background the spectral amplitude (grey) is shown.

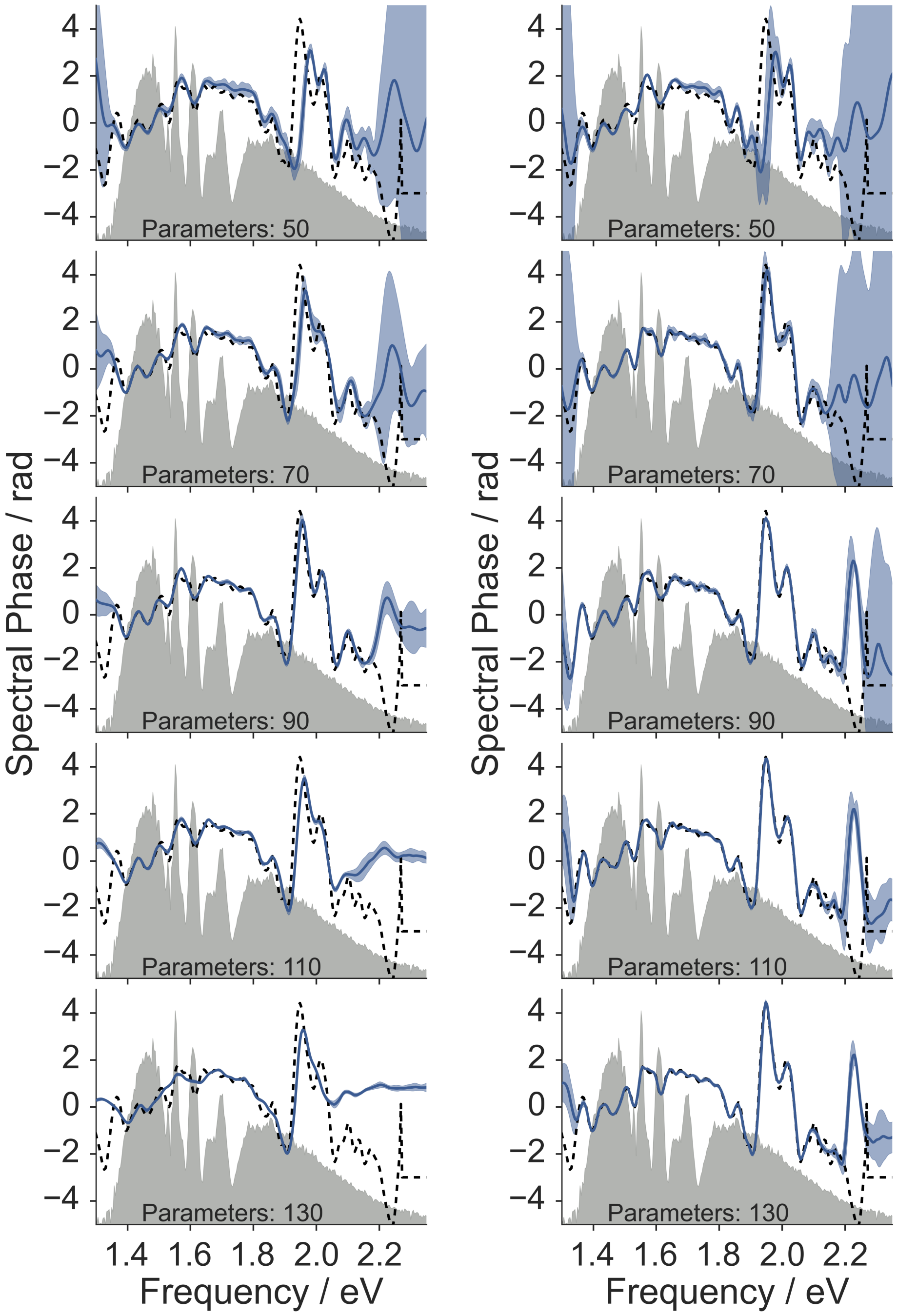

(a) Retrievals with 10 000 iterations. **(b)** Retrievals with 30 000 iterations.

Figure 3.15.: Mean spectral phase (blue) and its standard deviation (light blue) from ten consecutive retrievals performed on simulated data. The input phase, which is the same as in figure 3.11, indicated by the black dashed line. The number of parameters in the retrieval is increased from top to bottom. In the background the spectral amplitude (grey) is shown.

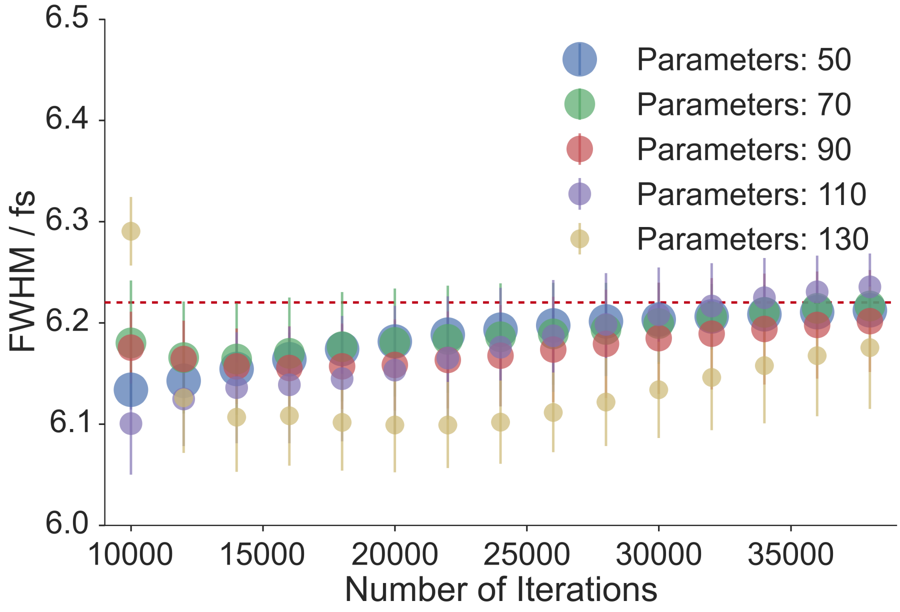

(a) FWHM data corresponding to figure 3.14.

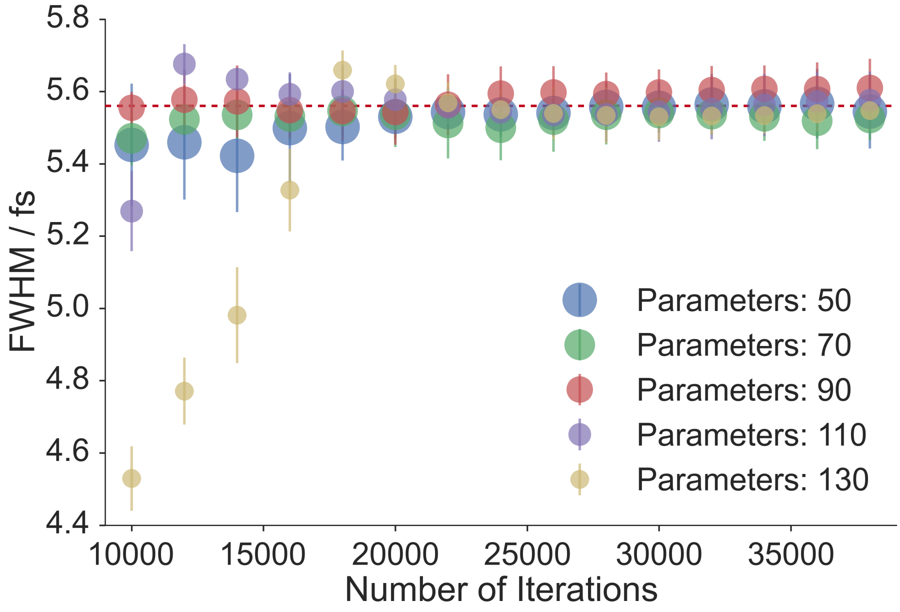

(b) FWHM data corresponding to figure 3.15.

Figure 3.16.: Full width at half maximum of the pulses, which are obtained from the spectral phases and amplitudes in the previous plots as a function of the number of parameters that built the phase functions and the number of iterations of the algorithm. The values which correspond to the input phases of the simulations are indicated by the red dashed lines.

3.6. D-Scan Measurements

This section shows actual results of D-Scan measurements. Four examples of pulse characterizations are shown and discussed. Further plots are attached in appendix A.2.2. It should be mentioned that the zero point of the glass insertion scale in the plots was set arbitrarily to the center of the traces main features. In addition, we performed a pressure scan of our hollow-core fibre to find out the optimum pressure. At each pressure setting, a D-Scan was performed. The results displayed in figure 3.19 show that the pulses are shorter and supported by a broader spectrum as the pressure increases. That is because the refractive index which induces the self-phase modulation in the gas scales with the density of the medium.

The D-Scan measurements also proved to be a valuable tool for the delicate alignment of the chirped-mirror compressor in the laser setup. To compensate for more glass insertion, the old compressor with five pairs of double-angle chirped mirrors was extended to seven pairs. The angle of incidence of the laser onto this kind of mirrors is extremely critical, as small deviations can introduce ripples onto the spectral phase[47]. Here, the D-Scan helped to check the alignment progress.

Figure 3.17a shows the D-Scan results of pulses with the flattest spectral phase, which we were able to produce and measure as part of this thesis. That the phase is well behaved can be seen in the raw data already: the trace has a strong horizontal symmetry.

Pulses with phase ripples as shown in figure 3.17b can be identified by the rippling structures along the spectral axis in the traces. The fast modulation of the spectral phase is most likely caused by a misalignment of the chirped mirrors regarding the angle of incidence.

In figure 3.18a it is obvious that the measurement was performed with a bad initial position of the glass wedges since only half of the trace is covered. In such a case, the wedges should be adjusted and a new measurement has to be performed. Nevertheless, the algorithm can still retrieve the spectral phase of the pulses, but these results have to be handled with care. The phase, which is depicted in the lower left plot and which leads to the temporal intensity in the lower right, is not necessarily the optimal phase. The algorithm only chooses among the phase functions, for which there is a corresponding glass insertion value in the data. If more/less glass has to be inserted into the beam to reach optimal pulse compression, the retrieval does not take notice of this. Surely, this scenario could be implemented and accounted for by the algorithm, but correcting the measurement is the better choice, since a retrieval from a trace with all features of the SHG signature will give better results.

The traces shown in figure 3.18b are strongly bend and the temporal intensity has a long pre-pulse. From simulations it is known that both of these effects are caused by a third-order phase component (see figures 2.2 and 3.1). No such component is present though in the retrieved phase or at least not clearly distinguishable. If the phase jumps at the wings of the spectrum were not present, it would be interesting to analyze the polynomial phase orders more thoroughly.

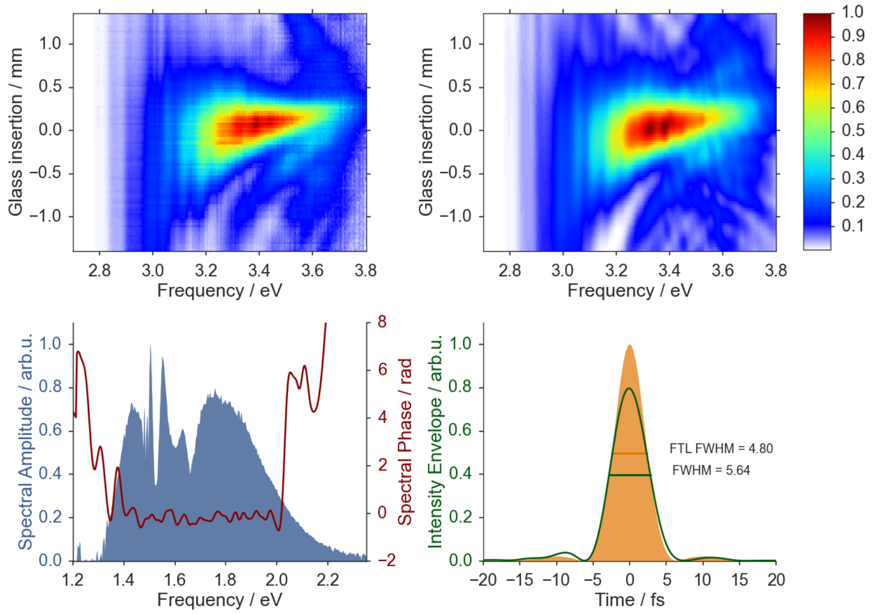

(a) Example of the D-Scan characterization of near transform limited pulses.

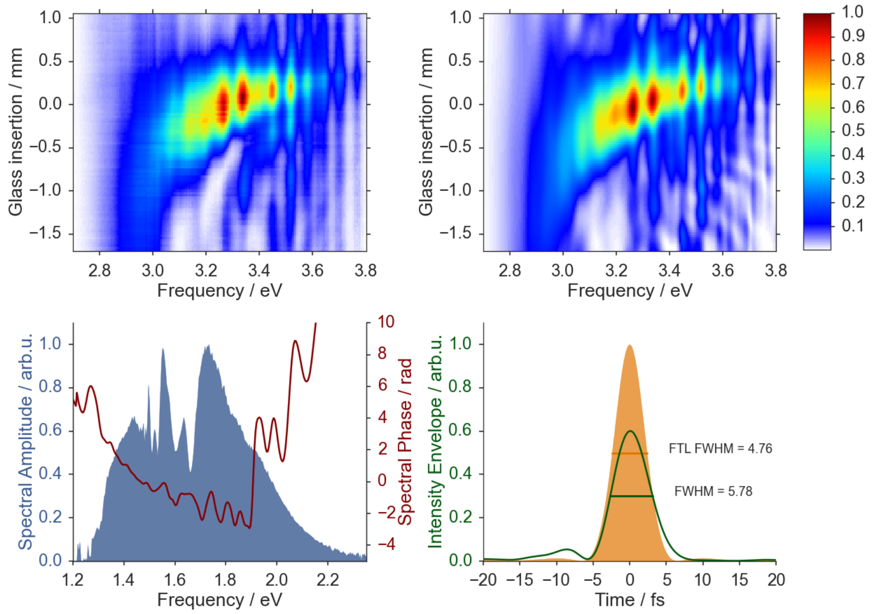

(b) Example of the D-Scan characterization of pulses with strong phase ripples.

Figure 3.17.: On top are the experimental (left) and retrieved (right) traces. On the bottom, the spectral fields (left) and the temporal pulse envelopes (right) are shown.

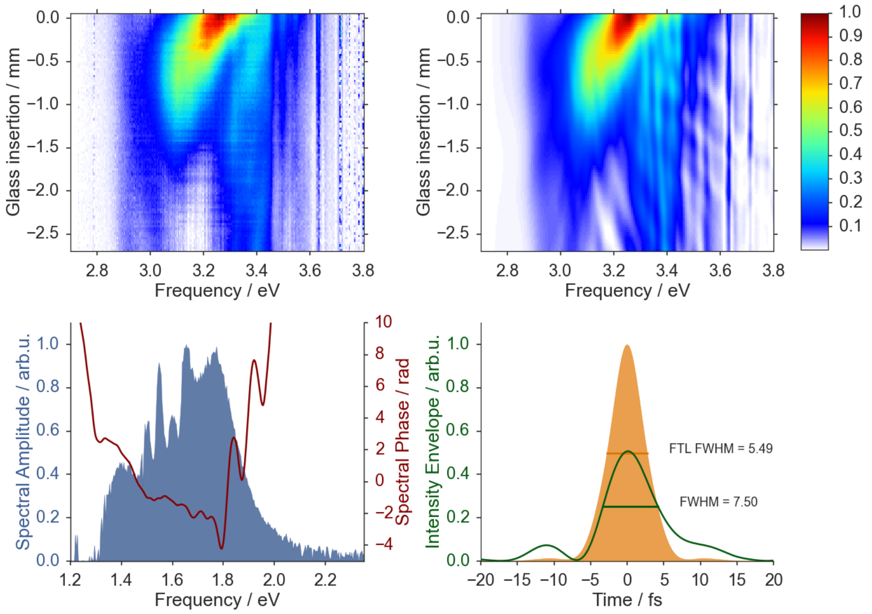

(a) Example of the D-Scan characterization with poor settings of the initial wedge positions.

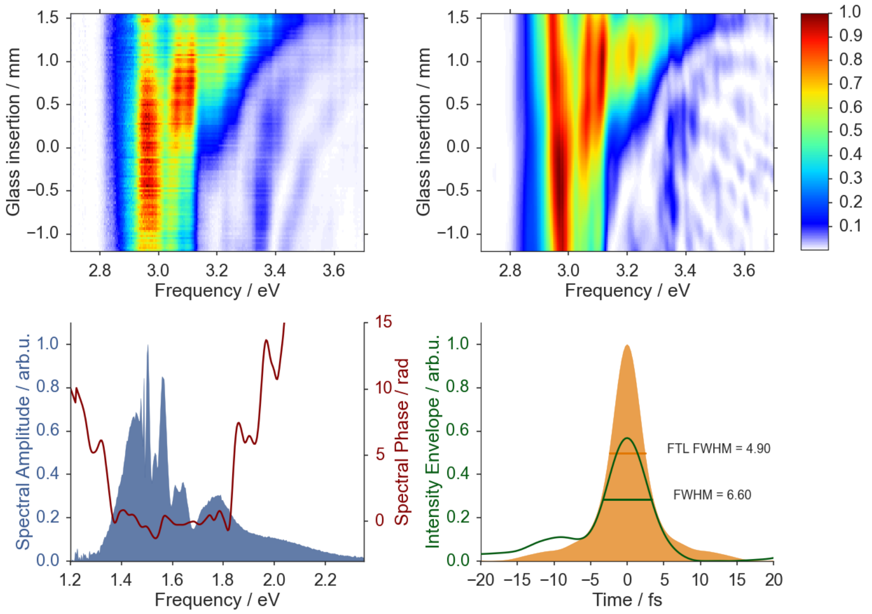

(b) Example of the D-Scan characterization of pulses with a rather spiky spectral amplitude.

Figure 3.18.: On top are the experimental (left) and retrieved (right) traces. On the bottom, the spectral fields (left) and the temporal pulse envelopes (right) are shown.

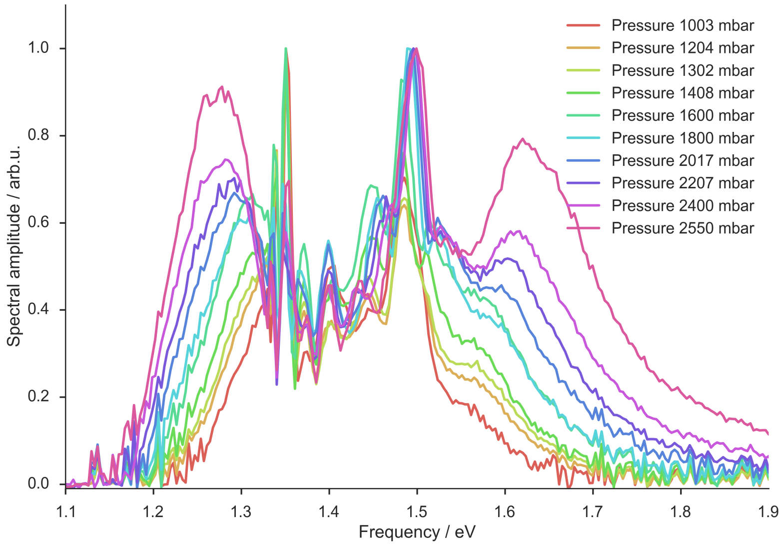

(a) Spectra acquiered during the pressure scan.

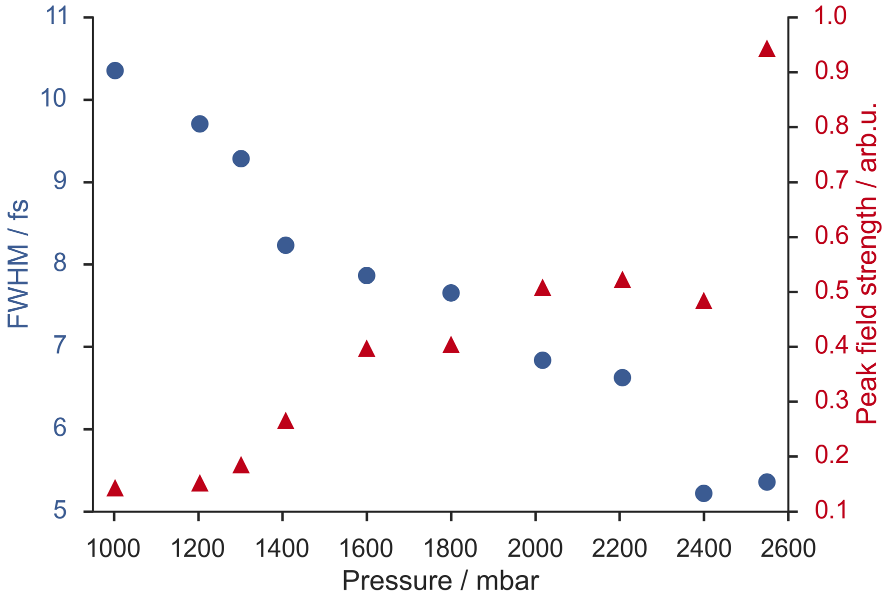

(b) Full width at half maximum and peak field strength of the pulses retrieved by the D-Scan for each pressure setting.

Figure 3.19.: Pressure scan data taken as the neon pressure inside the hollow-core fibre was increased from 1000 mbar to 2550 mbar.

4. Attosecond Streaking

In attosecond streaking—the method presented in this chapter—the oscillations of a strong laser field are sampled by sub-cycle photoelectron bunches and are mapped directly onto the electrons' kinetic-energy spectra. The photoelectrons are produced by ionization of a gas target by means of an attosecond XUV pulse from high-harmonic generation, which co-propagates with the NIR laser pulse. This technique does not only allow to directly observe the wave form of the laser's electric field, but can be extended to characterize the high-harmonic light, which triggers the probe electrons, as well. For the detection of the electrons typically a time-of-flight spectrometer is used. Such a device was designed and constructed in the frame of this work.

We call this method *attosecond streaking* as a reference to conventional streak cameras[1] and, because the fs-laser-field of the measured pulses is sampled with sub-cycle resolution. The fact that the electric field of the strong laser pulses varies considerably on timescales shorter than the optical cycle, which is $T_L = 2.5\,\text{fs}$ at the laser's center wavelength of 750 nm, is also the reason why methods like the ATR and FROG-CRAB reveal information about the temporal structure of the attosecond pulses. The related method of angular streaking is referred to as *attoclock*[10; 11; 43; 44] because it uses this as-resolution of fs-laser pulses to probe time delays in photoionization. Such time delays can also be investigated with attosecond streaking as demonstrated by Schultze et al. [45] for measurements in Neon.

Section 4.1 presents the theoretical background of attosecond streaking following the work by Goulielmakis et al. [19]. Furthermore, section 4.2 describes our design of the electron time-of-flight spectrometer (section 4.2.1), which is the key component of the experimental apparatus, the electron detector (section 4.2.2) and the signal extraction (section 4.2.3). A technical description of the streaking setup is summed up in section 4.3. For the current status of the

---

[1] Streak cameras are used to characterize light pulses as short as picoseconds ($1\,\text{ps} = 10^{-12}\,\text{s}$). Shining the pulses on a photocathode, time information on the photoelectrons is gained by mapping a time-dependent accelerating electric field to the spatial coordinate of a detector.

system and future measurement prospects, the reader is referred to the outlook in chapter 5.

4.1. Theoretical Background

In classical electrodynamics, the electric field is defined as the force per unit charge at a given point in space [25]. Consequently, the electric field of a strong laser pulse can be accessed by measuring the effect of this force $F = eE$ on an electron. The electrons are said to be streaked by the laser field, which throughout this chapter will be assumed to be linearly polarized. The experimental principles of attosecond streaking, which will be explained in the following, are sketched in figure 4.1.

As mentioned, the electron release is triggered by single-photon ionization of a gas target by means of an XUV pulse. In our experimental setup, the XUV pulse is generated by the strong NIR laser pulse itself via high-harmonic generation, which has the following two advantages. Firstly, the two pulses are synchronized and co-propagating, which allows to precisely control the production of the probe electrons in space as well as in time. Secondly, the introduction of a time delay between the two pulses is straightforward with a split-mirror setup[2]. In the experimental setup described here, the accuracy of the time-delay steps is of the order of 20 as—well below the duration of the XUV pulse itself.

After the ionization, the electrons have a certain kinetic energy W_0 and initial momentum p_0 according to $W_0 = \frac{p_0^2}{2m_e} = \hbar\omega_{XUV} - I_p$, where m_e is the electron mass, $\hbar\omega_{XUV}$ is the energy of an XUV photon and I_p is the ionization potential of the target gas. The XUV pulse inherently covers a certain bandwidth, which is mapped onto the kinetic energy spectrum of the electrons. In the region of temporal overlap between the two pulses, the probe electrons are set free by the XUV pulse and undergo fast oscillations, due to the ponderomotive force of the strong laser field. The final momentum of the electrons is not affected by their quivering motion in the presence of the field, but rather by the field's vector potential at their moment of birth. If we instantaneously place the probe electrons within the laser field at a moment τ_0, they experience the passage

---

[2] For a description of the high-harmonic beamline, into which the setup described here is implemented, see [42].

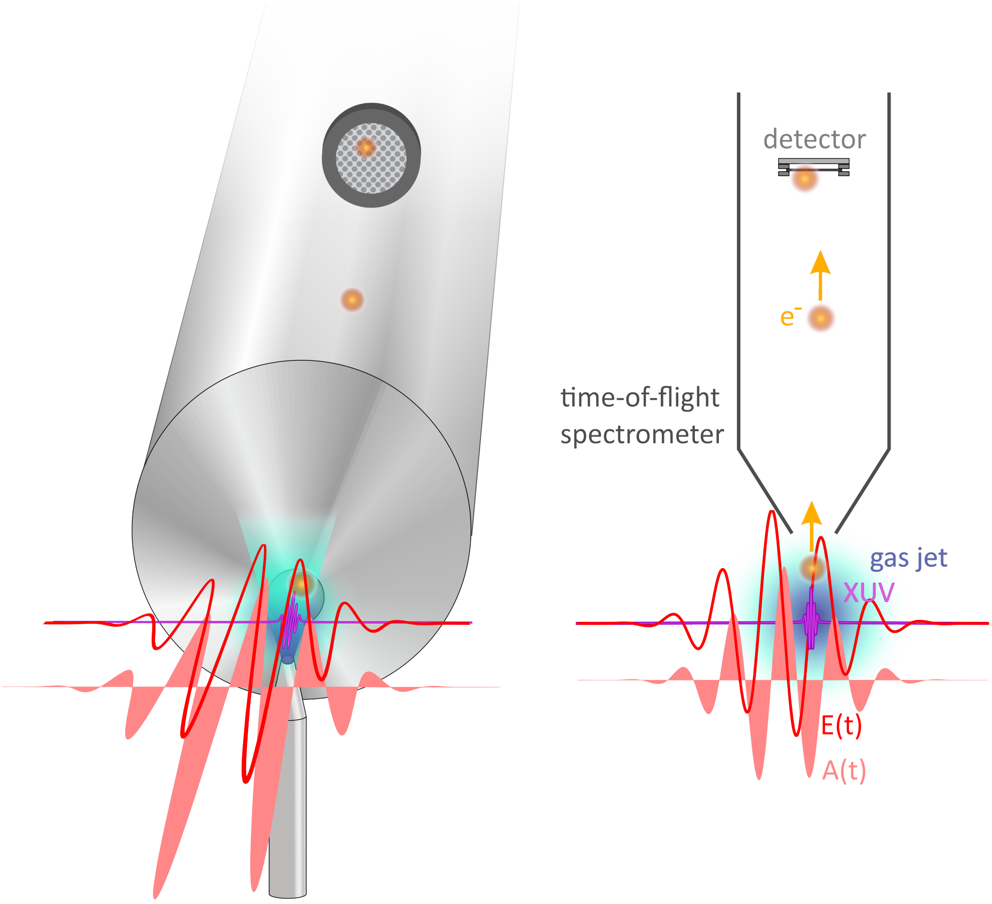

Figure 4.1.: The principle of attosecond streaking. Atoms emerging in a gas jet (turquoise) from a nozzle are ionized by an XUV pulse (violet) from high-harmonic generation. The freed electrons (yellow) probe the field of the strong laser pulses $E(t)$ (red) and receive a momentum boost depending on the corresponding vector potential $A(t)$. The momentum of the electrons parallel to the laser's axis of polarisation is measured using a time-of-flight spectrometer.

of the rest of the pulse, which induces a change of their momentum in the direction of polarization by $\Delta p(\tau_0)$:

$$\Delta p(\tau_0) = e \int_{\tau_0}^{\infty} E(t)\mathrm{d}t = eA_L(\tau_0), \tag{4.1}$$

where $A_L(t)$ is the vector potential of the electric field. We identify τ_0 as the time delay between the ionizing and the streaking pulse.

Thus, scanning the time delay and measuring the momentum shift Δp simultaneously, is equal to measuring the pulses' vector potential. If the latter is sampled fine enough, we can directly deduce the electric field by taking the derivative of $A_L(t)$ with respect to time,

$$E(t) = \frac{\partial}{\partial t} A_L(t). \tag{4.2}$$

Of course, the electrons are not generated instantaneously, because of the duration $\Delta\tau_{XUV}$ of the attosecond pulse. This uncertainty is mapped to an inaccuracy of the time delays between the laser pulse and the electrons, which are produced by the ionization. This smears out the measured vector potential, but does not invalidate the approximation. The pulses from HHG are inherently short $\tau_{XUV} < 1\,\mathrm{fs}$ and—except for the case of trains of attosecond pulses—still allow sensible sampling of the vector potential.

Because photoelectrons from the laser generated by multi-photon absorption affect the desired signal, the target gas has to resist strong-field ionization by the laser alone. Thus, noble gases such as helium or neon, which can still be ionized by the comparatively weak XUV pulse in a one-photon process, are suitable choices for the target.

4.1.1. Measurement Principle

In order to detect the electrons, an electron time-of-flight spectrometer oriented parallel to the streaking laser's axis of polarization is needed, by means of which the kinetic energy W of the electrons can be calculated. In absence of the streaking field, the kinetic energy is $W_0 = \frac{p_0^2}{2m_e}$. The momentum shift induced by the laser, translates to a shift of the kinetic energy of the electrons by $\Delta W \approx \frac{p_0}{m_e}\Delta p$. Thus, a large initial momentum of the electrons is desirable for a good energy resolution. To be precise, it is even necessary that the initial momentum is greater than the maximum momentum shift induced by the streaking laser $p_0 > |\Delta p_{max}|$. Otherwise, electrons would be streaked away from the detector for certain sampling positions of the laser's vector potential.

Experimentally, it is important to measure only electrons propagating along the laser's axis of polarization. The reason for this is that electrons that leave the interaction region at different angles may have the same kinetic energy, but reach the detector after different times-of-flight. Since the time-of-flight is needed to deduce the kinetic energy, this would smear out the measurable distribution of ΔW.

Because the momentum shift Δp has to be measured for different time delays and in order to obtain a good signal to noise ratio, the experiment cannot be performed with a single shot of the laser. This makes carrier-envelope phase stabilisation during the acquisition of a scan necessary, otherwise only CEP-averaged data is recorded. The result from a scan is a two-dimensional streaking trace, where the counts of detected electrons are plotted over the kinetic energy of the electrons and the time delay between the ionizing and the streaking pulse. The expected traces for both cases—measurements with and without CEP stabilisation—are illustrated in figure 4.2.

From figure 4.2 it is evident that the largest possible change in kinetic energy ΔW_{max} has to be at least as large as the spectral width covered by the XUV pulse. For this to be true, the peak strength of streaking field needs to be sufficiently strong. If we demand that $W_0 = 50\,\mathrm{eV}$ and $\Delta W_{max} = 15\,\mathrm{eV}$ and approximate equation 4.2 for the peak field strength as

$$E_{max} \approx \frac{2A_{Lmax}}{T_L/2}, \tag{4.3}$$

we find an estimate of the peak electric field strength E_{max} needed for streaking:

$$\begin{aligned} E_{max} &\approx \frac{\Delta W}{eT_L}\sqrt{\frac{8m_e}{W_0}}, && (4.4)\\ &\approx 8 \cdot 10^7\,\mathrm{V/cm}, && (4.5) \end{aligned}$$

which corresponds to an intensity of $I \approx 4 \cdot 10^{13}\,\mathrm{W/cm^2}$. These field strengths are within the accesible range of the setup presented in section 2.3.

Since the spectrometer measures the time-of-flight of the electrons, the momentum of the electrons is easily calculated by taking the known distance from

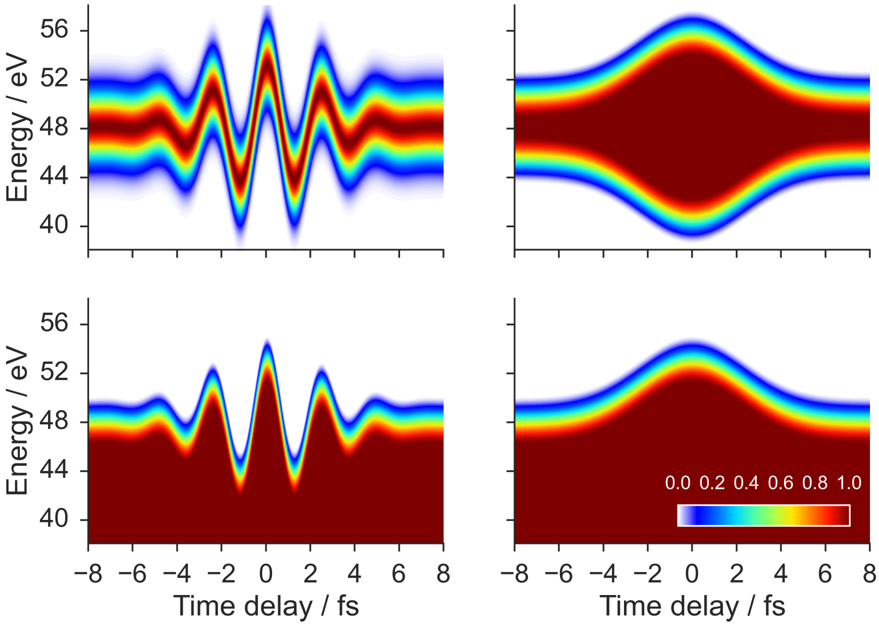

Figure 4.2.: Illustrations of possible streaking traces, where electron counts (colorscale in arbitrary units) are plotted over the kinetic energy of the electrons and the XUV-NIR time delay. On the left, the CEP of the laser is stabilized, on the right the effect expected for a washed out CEP is demonstrated. Assuming the ionization potential of helium, in the top row, the XUV beam used is bandpass filtered to span 8 eV around a center energy of 72.7 eV. The bottom row illustrates measurements we expect for harmonics lowpass filtered by transmission through aluminium, which has a cutoff at 72.7 eV (see figure 4.3). Effects of atomic resonances are not considered here.

the interaction region to the detector into account. If there was nothing more to it, this would suffice to access the laser's vector potential. The need to compute the kinetic energy arises, because the time-of-flight has to be calibrated. Experimentally, the time-of-flight is recorded by a timer, which is started by a trigger from the laser and stopped by signals from the detector. The start of the timer can be set off by the signal of a photodiode somewhere along the laser's beam path. The laser pulses then propagate to the experiment, generate the XUV pulses, which themselves propagate further to set initiate the real reaction to be recorded by ionizing the gas target. The false offset the timer

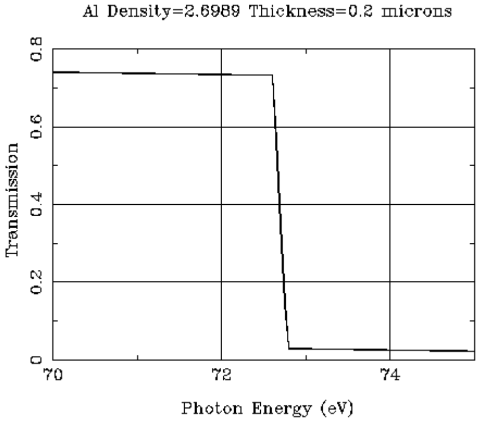

Figure 4.3.: Photon transmission spectrum of a 0.2 µm thin aluminium filter between 70–75 eV. The transmission window, which closes here, opens at ~18 eV. Data from online service provided by [20].

measures, because the pulses and electric signals take time to propagate, has to be accounted for. Else the timing unit with its 1 ns resolution, would introduce errors as soon as the pulses have to travel further than 30 cm to the interaction region. This timing offset is calibrated by matching the kinetic energy spectra of the electrons recorded in the absence of the streaking laser to the spectrum of the XUV pulse according to $W_0 = \hbar\omega_{XUV} - I_p$. In work presented in literature [18; 29; 19], the high–harmonics are bandpass–filtered and thus their spectrum is known. In the setup described here, an XUV spectrometer at hand allows to directly monitor the XUV spectrum. Another approach illustrated in figure 4.2 makes use of the spectral properties of an aluminium filter in the beam path of the HHG radiation. The XUV transmission window of aluminium closes abruptly at 72.7 eV (see figure 4.3). In the electron spectrum, this edge should be mapped onto the fastest electrons and can then be used for calibration as well.

4.2. The Electron Spectrometer

The following sections turn towards the practical details of time-of-flight electron spectroscopy. The design of the spectrometer, which was planned and constructed as part of this thesis, is explained in section 4.2.1. Section 4.2.2

focuses on the working principle of the electron detector, while section 4.2.3 illustrates how the data acquisition works.

4.2.1. Spectrometer Design

The essential considerations for the design of the electron time-of-flight spectrometer were threefold. (1) The positioning of the spectrometer must be flexible in order to align it with the focus of the laser and the XUV. (2) Its inside has to be field free, such that the flight of the electrons is not perturbed by external electromagnetic fields. (3) The vacuum in the spectrometer arm has to be good enough for the electron detector to be operated safely and the electrons to reach the detector.

The first point demanded the use of large manipulators, one for the lateral and one for the axial movement. The advantage of having these manipulators resides in the flexibility they grant to the setup. Instead of having to move the focal spot towards the spectrometer entrance, it can easily be adjusted by hand, while a long-focal length microscope camera is used to monitor the tip of the spectrometer. This way, no changes to the existing beamline had to be made and it can in principle now be operated with the new electron spectrometer and the old XUV spectrometer in dual operation mode[3].

The need to keep the spectrometer free from stray electric and magnetic fields arises, because they might deflect the electrons on their way to the detector. The flying electrons are moving charged particles, whose straight trajectories would be bent due to the Lorentz force caused by the earth's magnetic field and the remaining magnetization of the vacuum chambers, if left unshielded. This in turn might either alter the electrons' time-of-flight or lead them astray such that they do not reach the detector at all. Therefore, a μ-metal tube with a conical tip encloses the flight path from the interaction region to the detector. μ-metal is a special alloy, which—after undergoing thermal postprocessing—has an enormous magnetic permeability μ. Because of this, magnetic field lines from the outside are trapped in the metal and do not penetrate the inside of the spectrometer, which leads to the desired shielding. In order to shield the electrons from electric fields from the electrodes of the detector, a fine mesh on ground potential will be set up in front of the detector stack. Thus, all unwanted electric and magnetic fields are taken care of.

---

[3] Also referred to as BADASS (*Badass Attosecond Dual (Absorption & Streaking) Spectrometer*)

The last requierement on the design is that the pressure at the position of the detector must be kept below $2 \cdot 10^{-6}$ mbar during operation. The reason for this is that the electron detector, which is build from two micro-channel plates (MCPs) and an anode, operates at high voltages (HV) and is easily destroyed under bad vacuum conditions. Additionally, lower pressures implicate a larger mean free path of the electrons, which preferentially should exceed the dimensions of the spectrometer. However, during absorption and streaking measurements, the backgrond pressure in the experimental chamber is typically in the range of 10^{-3} mbar and even higher close to the gas target. Therefore the μ-metal shield was designed to act as a partition between the main experimental chamber and the inside of the spectrometer. The tip of the shield has an entrance aperture with a diameter of only 1 mm, which acts as a differential pumping stage beneficial to keep the pressure low and also helps to select the electrons that leave the interaction region in a small solid angle pointed towards the detector. By mounting a turbo molecular pump (HiPace 300, Pfeiffer Vacuum) behind the detector, the spectrometer volume can easily be held at pressures well below the operation requirements of the MCPs. In fact, at backing pressures of ~200 mbar in the gas nozzle and 10^{-3} mbar in the experimental chamber, the inside of the spectrometer still maintained $2.1 \cdot 10^{-7}$ mbar. In the future, this will enable to do electron streaking and XUV absorption measurements at the same time.

4.2.2. The Detector

The electron detector from the company Roentdek is sketched in figure 4.4. It consists of two MCPs and an anode plate, to all of which different, electric potentials are applied. A single MCP is a 0.3 mm thin disk perforated by an array of microscopic channels, which have a pore diameter of 6 µm. Because the microchannels have a small bias angle with respect to the surface normal, the electrons cannot pass the MCPs without impinging on their walls. When an electron first hits the wall of a pore, it creates secondary electrons, which start an avalanche process that leads to the amplification of the electron signal. Thus, every pore acts as an electron multiplier.

In the case of the detector described here, two MCPs were mounted on top of each other, such that the electron avalanche from the front MCP is further amplified by the back MCP. They are aligned in such a way that the

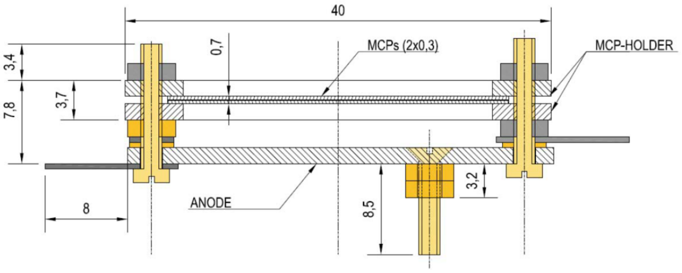

Figure 4.4.: Sketch of a cut through the detector. The whole detector has a diameter of 40 mm with an active area of 25 mm diameter. The yellow screws and nuts are made of plastic in order to provide isolation. Taken from a test report by Roentdek.

microchannels of the two plates have opposite bias angles. This configuration is called a chevron stack, because the channels form a V-shape.

In order to reach high enough signal amplification and good detection efficiency, all components have to be held at specific high–voltage levels. During first test measurements, the MCP front was held at 300 V, the MCP back at 2400 V and the anode at 2700 V. In principle, the signal can be picked from any of the parts above by means of an RC-output coupler. The signals from the anode have a FWHM of ~3 ns (see figure 4.5) and seemed to be well behaved.

A single pore of the MCP has a dead time of a couple of nanoseconds, because it needs to refill its charge after the current drain by the signal. But in terms of timing resolution this should not affect us, since it is very improbable to hit the same spot on the detector twice by two consecutive electrons at the low count rates of 1-10 events we expect per shot of the laser. The time resolution of the signal digitizer to be treated in the next section is more critical .

With the detector working satisfactorily, the next step is to expand it by adding a grounded mesh in front of the MCP stack. In the current configuration, the electrons are accelerated by the electric field between the MCP front (positive potential) and the entrance aperture of the spectrometer (ground potential). Since this leads to a guiding of the electrons and shifts their natural kinetic energy, the energy resolution would suffer under the current circumstances, because the electrons have a shorter time-of-flight. This effect can be avoided by shielding the MCP by means of an optically thin mesh on ground potential.

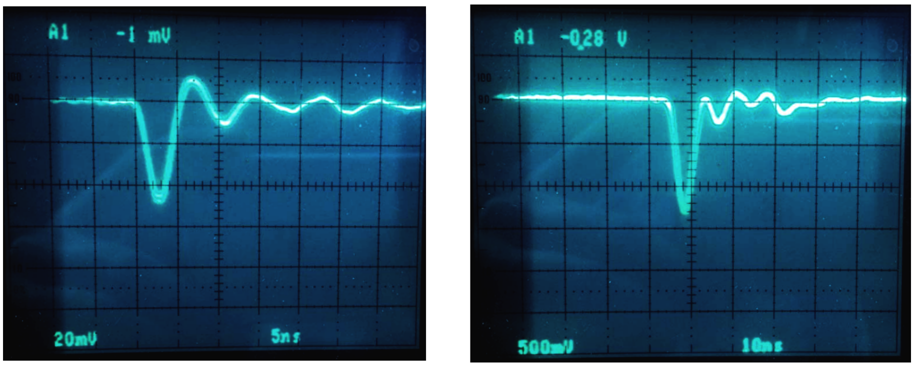

Figure 4.5.: Typical signal from the MCP back (left) and anode (right). The anode signal is amplified by a factor of 50. Taken from test report by Roentdek.

4.2.3. Signal Processing

When an electron hits the detector, a cascade of secondary electrons is released and amplified as described above. This signal is strong enough to be outcoupled by an RC-coupler which isolates the ac signal from the dc electrode potential. Following this, the signal pulses are further amplified by a factor of 200 in a fast amplifier (FTA 820a, Ortec) and converted to standardized NIM pulses[4] by a *constant fraction discriminator* (CFD). After the amplifier, the raw pulses have FWHM durations of ~5 ns and look similar to the pulses displayed in figure 4.5. The CFD has the important task to process the raw signals and assign a meaningful timestamp to them which, as we discussed in section 4.1.1, is used as the stop signal for the time-of-flight measurement timer. The pulse shape itself is neither processible by other devices nor reproducible. The operation, which the CFD performs and which leads to its name, is to detect the position at the rising edge of the pulse where the pulse has reached a given constant fraction of its total height. This is equivalent to finding the pulses maximum independently of the actual height. It then launches a normed pulse, which marks this position. This way the important timing information is transferred to a more robust type of signal.

The last element in the measurement chain is a time digitizer PC card for the acquisition of the time-of-flight information. This so-called scaler card

---

[4] The Nuclear Instrumentation Module (NIM) standard provides mechanical and electrical definitions for modular instrumentation devices.

(P7888, Fast ComTec GmbH) has two analog inputs—the trigger taken from the laser (start) and the signal from the electron detector (stop)—and is specifically designed for the acquisition of time-of-flight spectra. Its work cycle is started by a trigger signal. According to the settings, this opens a time window in which the card expects stop signals. The start and end of this window are programmable over a wide range and will have to be determined experimentally. When no stop signal is recorded, the work cycle starts anew with the next trigger pulse. For each time-delay setting the measured events are binned in a histogram by the software provided with the card producing different time-of-flight spectra. This software can be controlled via Labview by using a *dynamic data exchange* (DDE) protocol. A Labview VI that controls both the time-delay piezo and the data acquisition of the scaler card is already set up.

With the data transferred to Labview, the time-of-flight spectra are to be converted to kinetic energy spectra according to:

$$
\begin{aligned}
E_{kin} &= \frac{m_e}{2}\left(\frac{l}{t-t_0}\right)^2 & (4.6)\\
&= \big((t-t_0)/\mathrm{ns}\big)^{-2} 1.023\,413\,4 \cdot 10^6\ \mathrm{eV}, & (4.7)
\end{aligned}
$$

where $l = 60\,\mathrm{cm}$ is the distance from the tip of the spectrometer to the detector and t_0 is the constant offset of the trigger that is discussed in section 4.1.1. In the latter equation the conversion to electron volts is already included.

Regarding time resolution, the scaler card becomes the limiting factor of the whole detection setup as it can only record histograms with a smallest bin width of 1 ns, which corresponds to a sampling rate of 1 GHz. For electrons, which are detected with a kinetic energy of 50 eV and therefore have a time-of-flight of ~ 143 ns, this corresponds to an energy resolution of ~ 0.7 eV. For electrons with lower kinetic energy the time-of-flight is longer and thus the energy resolution becomes better. However, there is a tradeoff between the energy resolution and the amplitude of the streaking shift in kinetic energy ΔW which scales with the initial momentum of the electrons (see section 4.1.1). Eventually, the spectral filter for the XUV radiation will determine the properties of the electron bunches (see figure 4.2).

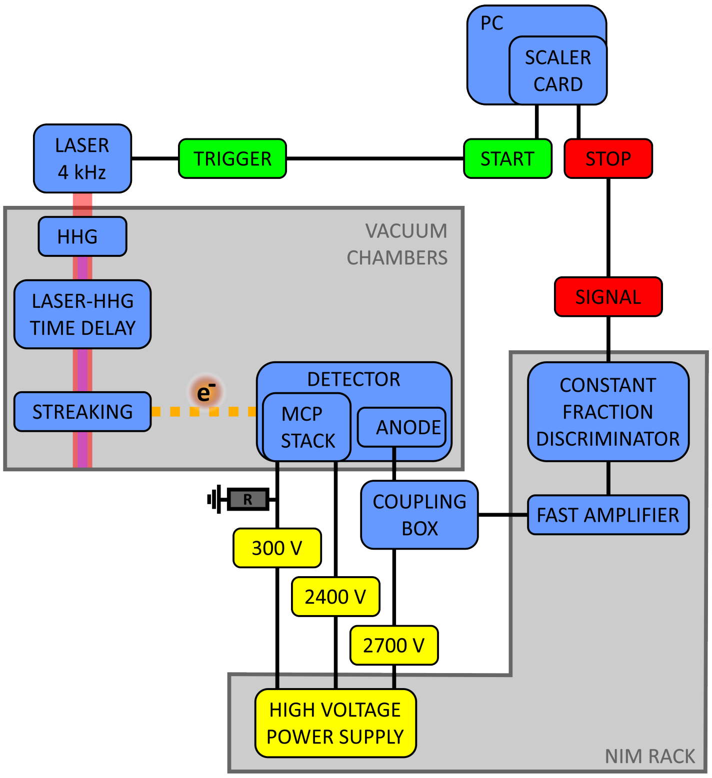

Figure 4.6.: Sketch of all components, which are part of a streaking experiment. While the vacuum chambers are mounted on an optical table, most of the read-out electronics are housed in a standardized NIM rack, which acts as their power supply.

4.3. Experimental Setup

The last section explained in detail the overall working principle of the streaking setup and its individual components. In order to see the larger picture, figure 4.6 gives an overview of all the parts involved in a streaking measurement. The spectrometer as a whole is depicted in figure 4.7. For completeness, some more detail information is provided in the following.

4.3.1. Power Supply

High-voltage levels have to be applied to the MCP front and back and the anode of the detector. The MCP front is supplied with 300 V, because this maximizes

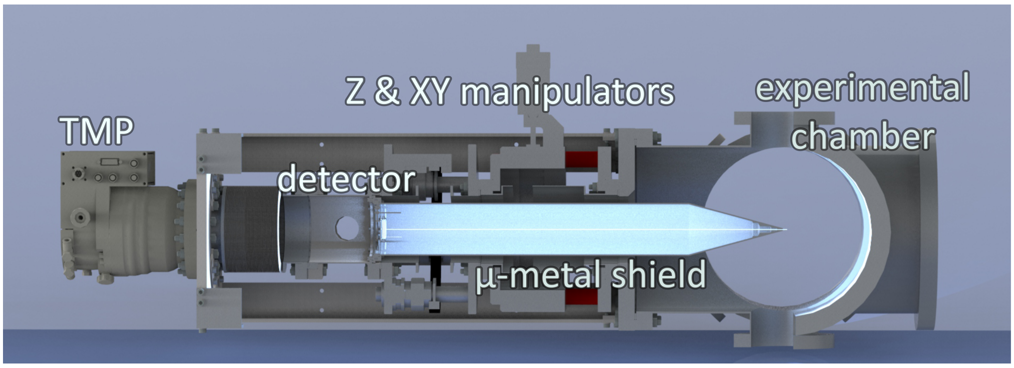

Figure 4.7.: Rendered cut through the time-of-flight spectrometer. The perfect flight path of the electrons, which is depicted as the white line in the middle of the μ-metal tube, is 60 cm long. The separation of the low pressure region of the spectrometer (light blue) to the experimental chamber is evident.

the detection efficiency of electrons. The power supply used for the front can deliver 2 kV and a current of 6 mA (NHQ 202M, ISEG), while MCP back and anode could be supplied with up to 6 kV/2 mA (NHQ 206L, ISEG). During the test measurements run so far, the voltage / current at the detector were 302 V/4 µA at the MCP front, 2405 V/50 µA at the MCP back and 2700 V/0 µA at the anode. The current through the MCPs is non-zero because the MCP stack has a finite resistivity of ~55 MΩ. As a result, the high voltage applied to the MCP back does not drop over the MCP stack and would be fed into the power supply of the MCP front. To prevent the latter from happening and to be able to regulate the voltage on the MCP front independently from the back, the MCP front is connected to ground via a 6 MΩ resistor (see figure 4.6). This way the resistor acts as one arm of a voltage divider and drains the majority of the current from the MCP back. The power supply of the MCP front can now easily counter the rest of the voltage that is applied to it by the other power supply.

When the high voltages are applied to the MCP back the first time after the vacuum chambers have been vented, special care should be taken to ensure that the MCP resistivity is unchanged, e.g. the current should be monitored each time the voltage is raised and it should rise linearly with the voltage according to Ohm's law. Furthermore, the potential difference between the MCP back and the anode should never exceed 500 V and the anode current should stay at 0 µA at all times.

4.3.2. Test Measurements

In order to align the μ-metal drift-tube, a long-focal length microscope camera in front of an acrylic glass flange is pointed onto a mirror on the inside of the vacuum chamber. This gives visual access to a sideview of the tip of the spectrometer and the gas nozzle. By shining an adjustment laser (HeNe) onto the nozzle, the z-manipulator and the vertical axis of the xy-manipulator can be set to the right position. For the adjustment of the horizontal axis, we irradiated the side of the gas nozzle with the XUV pulses, which knocked a large amount of electrons out of the metal. Moving the spectrometer, this signal could then be maximized by monitoring it on a GHz-oscilloscope (LeCroy). For further fine adjustments of the horizontal axis we used the actual signal from the gas jet. Picked up directly from the anode, these signals looked similar to the ones shown in figure 4.5, which proves that the detector is working fine.

5. Summary and Outlook

The emphasis of this work is placed on the characterization of ultrashort fs-laser pulses with the main objective being the implementation of a dispersion scan (D-Scan) and an attosecond streaking setup. Both characterization methods were installed and tested, and the D-Scan has already proven to be a valuable tool in everyday laboratory routine. Because the two techniques differ substantially from each other in in terms of requierements, benefits and operation principles, they will be reviewed separately in the following sections.

5.1. Dispersion Scan

A pulse characterization with the D-Scan consists of the acquisition of the measurement data and the phase retrieval by an iterative algorithm, both of which take about 3 min. It has been employed to optimize the delicate alignment of a chirped–mirror compressor, to check the performance and optimal gas pressure of a hollow-core fiber, and to monitor and optimize the day-to-day trend in the performance of the laser system.

At the heart of this method is the retrieval algorithm, which was tuned and tested in order to yield stable results. Its parallelization proved to be extremly valueable as it allowed to test parameter regimes, which were beyond practical limits of retrieval times before. The evaluation showed that good phase retrievals can be expected if the algorithm is run with 100 phase parameters and at least 20 000 iterations. The error of the FWHM of the characterized pulses is estimated to be ± 0.2 fs.

The evaluation showed that traces with lower sampling of the glass insertion do not alter the performance of the retrieval, which could be used in the future to speed up both, the measurement and the algorithm by approximately a factor of two.

In order to decouple the D-Scan from a specific position within a single laser system, an expansion of the setup is currently under consideration. By adding a small chirped-mirror compressor and using glass wedges, which are independent of the laser system, the D-Scan can become a stand-alone application. This may be the only way to include it in laser systems with less precompensated glass insertion as is usually the case when dealing with sub-two-cycle laser pulses.

5.2. Attosecond Streaking

With the electron time-of-flight spectrometer, which is the principle component of the attosecond streaking setup, the *attosecond transient absorption spectroscopy* (ATAS) beamline has gained a powerful new feature to access the dynamics of atomic and molecular quantum systems. First tests have shown that the detector and the signal electronics work as expected.

The next step to a fully functional setup will be the addition of a mesh to be placed in front of the detector in order to shield electrons from the potential of the MCP front, which is currently under construction. Further improvements could envisage a new design for the gas nozzle of the gas target. Reports from leading groups in the field of attosecond streaking [18; 46] are that glass nozzles coated with graphite are more suitable than the current steel nozzle to keep the interaction region in front of the spectrometer free from stray electric fields. Finally, the spectrometer resolution could be improved by slowing the electrons down by means of a retarding potential in front of the drift tube [12].

Parameters which have yet to be determined experimentally include the electron count rate and thus the time it takes to record a full time-of-flight spectrum as well as the duty cycle of the scaler card. Furthermore, it will be intriguing to find out whether we can rely on the edge in the spectral transmission of the aluminum filters (see figure 4.2) as a spectral filter.

Regarding the processing of the data, it should be straightforward to extract the shape and duration of the NIR laser pulses. More involved analyses to extract information on the HHG pulses will either make the implementation of a FROG CRAB algorithm [34] or an adaption of the D-Scan algorithm necessary.

Provided all of the requierements above are met, the attosecond streaking will not only be a technique for an *in situ* measurement of the NIR laser pulses but a complement to the ATAS XUV spectrometer. The latter has access to bound-bound transitions in atoms and molecules and the effects of strong laser fields on the dynamics of bound electrons, whereas attosecond streaking takes hold of the freed electrons. A first test measurement could be the repetition of measurements of autoionizing states in helium described by Blättermann et al. [1] with the simultaneous capture of the photoelectrons. Such a comparison has not yet been reported experimentally and only recently been done in theory [54]. Even though the investigation of autoionizing states by streaking techniques has already been conducted in theory [51; 53; 4; 26] and experiment [16; 50], we are confident that our dual approach may serve to gather new insights. Finally, it should be mentioned that such dual measurements have not yet been performed and will be feasible with our setup only because of the highly efficient differential pumping stage.

A. Appendix

A.1. Phase Dependence of the D-Scan Trace

This appendix proves the independence of the D-Scan trace from constant and linear phases.

Starting out from the analytic expression given by equation 3.1 and writing the spectral field in terms of amplitude and phase following equation 2.5, yields:

$$\begin{aligned} S(\omega, z) &\propto \left| \int \left(\int E(\Omega) e^{izk(\Omega)} e^{i\Omega t} \mathrm{d}\Omega \right)^2 e^{-i\omega t} \mathrm{d}t \right|^2 \\ &\propto \left| \int \left(\int A(\Omega) e^{i\varphi(\Omega)} e^{izk(\Omega)} e^{i\Omega t} \mathrm{d}\Omega \right)^2 e^{-i\omega t} \mathrm{d}t \right|^2 \end{aligned}$$

As in equation 2.18, the spectral phase is expressed as a taylor series up to the second order $\varphi(\omega) = \varphi_0 + \tau_0 \omega + \mathit{\Phi}(\omega)$.

$$S(\omega, z) \propto \left| \int \left(\int A(\Omega) e^{i(\varphi_0 + \tau_0 \Omega + \mathit{\Phi}(\Omega))} e^{izk(\Omega)} e^{i\Omega t} \mathrm{d}\Omega \right)^2 e^{-i\omega t} \mathrm{d}t \right|^2$$

Next, the inner square product, which represents the SHG, is written out explicitly:

$$
\begin{aligned}
S(\omega, z) \propto & \left| \int \left(\int A(\Omega_1) e^{i(\varphi_0 + (\tau_0 + t)\Omega_1 + \varPhi(\Omega_1) + zk(\Omega_1))} \mathrm{d}\Omega_1 \right. \right. \\
& \left. \left. \times \int A(\Omega_2) e^{i(\varphi_0 + (\tau_0 + t)\Omega_2 + \varPhi(\Omega_2) + zk(\Omega_2))} \mathrm{d}\Omega_2 \right) e^{-i\omega t} \mathrm{d}t \right|^2 \\
\propto & \left| \int \mathrm{d}t \left(\int \int \mathrm{d}\Omega_1 \mathrm{d}\Omega_2 \; A(\Omega_1) A(\Omega_2) e^{2i\varphi_0} e^{iz(k(\Omega_1)k(\Omega_2))} \right. \right. \\
& \left. \left. \times \; e^{i(\tau_0(\Omega_1 + \Omega_2) + \varPhi(\Omega_1) + \varPhi(\Omega_2))} e^{i(\Omega_1 + \Omega_2)t} \right) e^{-i\omega t} \right|^2
\end{aligned}
$$

The term with the constant phase can be drawn out of the integrals and cancels due to the absolute value.

$$
\begin{aligned}
S(\omega, z) \propto & \left| \int \int \int \mathrm{d}t \mathrm{d}\Omega_1 \mathrm{d}\Omega_2 \; A(\Omega_1) A(\Omega_2) e^{iz(k(\Omega_1)k(\Omega_2))} \right. \\
& \left. \times \; e^{i(\tau_0(\Omega_1 + \Omega_2) + \varPhi(\Omega_1) + \varPhi(\Omega_2))} e^{i(\Omega_1 + \Omega_2 - \omega)t} \right|^2
\end{aligned}
$$

Now we see that the last exponential factor and the integral over $\mathrm{d}\Omega_2$ are the definition of the Dirac δ-distribution: $\delta(\Omega_2 = \omega - \Omega_1) = \int \mathrm{d}\Omega_2 e^{i(\Omega_1 + \Omega_2 - \omega)t}$. With this we find:

$$
\begin{aligned}
S(\omega, z) \propto & \left| \int \int \mathrm{d}t \mathrm{d}\Omega_1 \; A(\Omega_1) A(\Omega_2) e^{iz(k(\Omega_1)k(\Omega_2))} \right. \\
& \left. \times \; e^{i(\tau_0(\Omega_1 + \omega - \Omega_1) + \varPhi(\Omega_1) + \varPhi(\omega - \Omega_1))} \right|^2
\end{aligned}
$$

$$S(\omega, z) \propto \left| \int\int \mathrm{d}t\mathrm{d}\Omega_1 \; A(\Omega_1)A(\omega-\Omega_1)e^{iz(k(\Omega_1)k(\Omega_2))} \right.$$
$$\left. \times \; e^{i(\tau_0\omega+\mathit{\Phi}(\Omega_1)+\mathit{\Phi}(\omega-\Omega_1))} \right|^2$$

Since now $\tau_0\omega$ is also only a constant phase, it can be pulled out and vanishes. The result has no dependence on constant and linear phase orders anymore:

$$S(\omega, z) \propto \left| \int\int \mathrm{d}t\mathrm{d}\Omega_1 \; A(\Omega_1)A(\omega-\Omega_1)e^{iz(k(\Omega_1)k(\Omega_2))} \right.$$
$$\left. \times \; e^{i(\tau_0\omega+\mathit{\Phi}(\Omega_1)+\mathit{\Phi}(\omega-\Omega_1))} \right|^2$$

A.2. Supplementary D-Scan Plots

A.2.1. Consistency Measurements

By comparing figures A.1, A.2 and A.3 to figures 3.7, 3.8 and 3.9 on pages 36-38, it was found that D-Scan measurement and retrievals with half the ususal sampling rate yield the same results within the bounds of the error of the algorithm.

A.2.2. Example D-Scan Characterizations

Further exemplary D-Scan characterizations are illustrated in figures A.4 and A.5 on pages viii and ix.

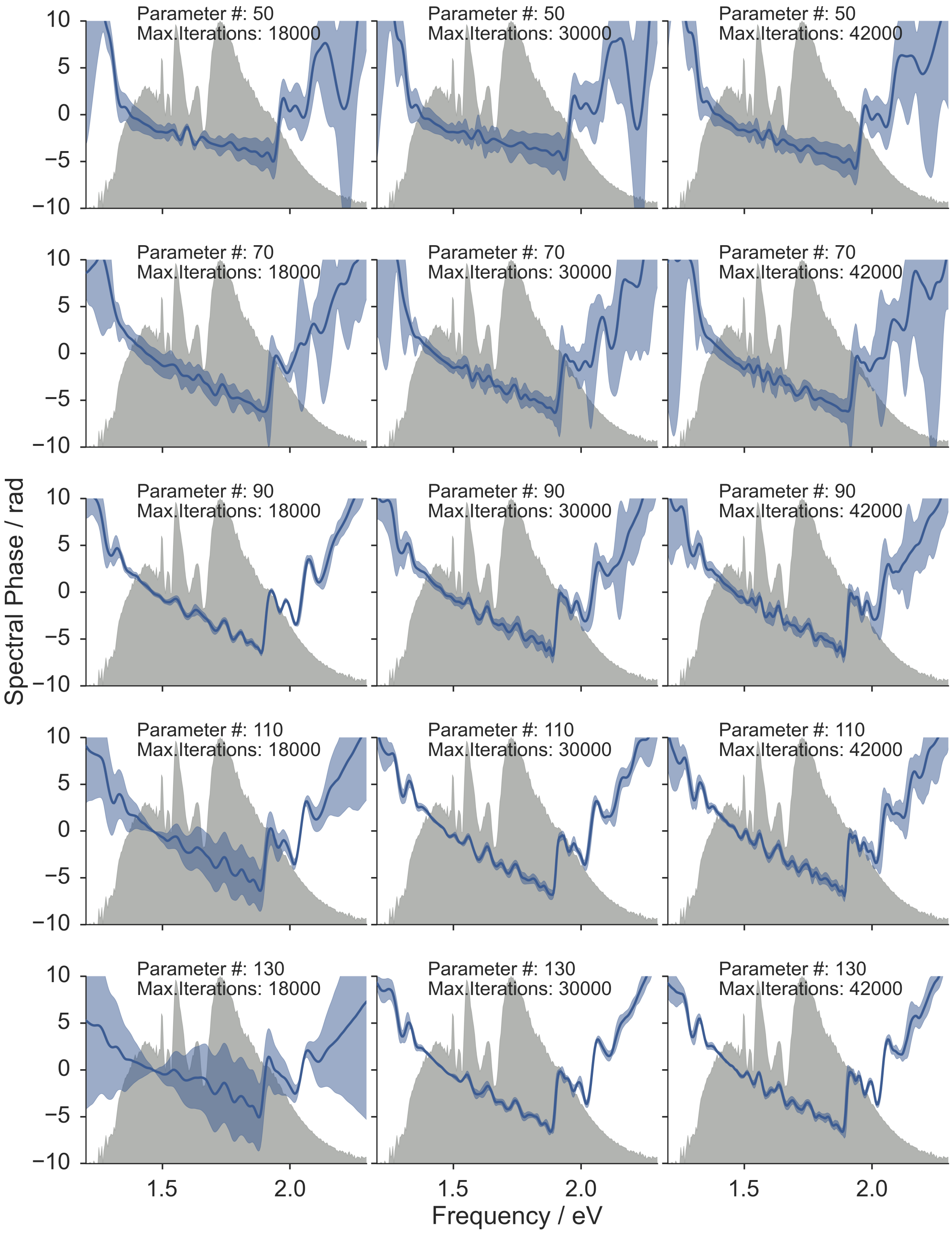

Figure A.1.: The same plots as in figure 3.7, with the difference that the measured data was sampled with half the number of steps in the glass insertion axis.

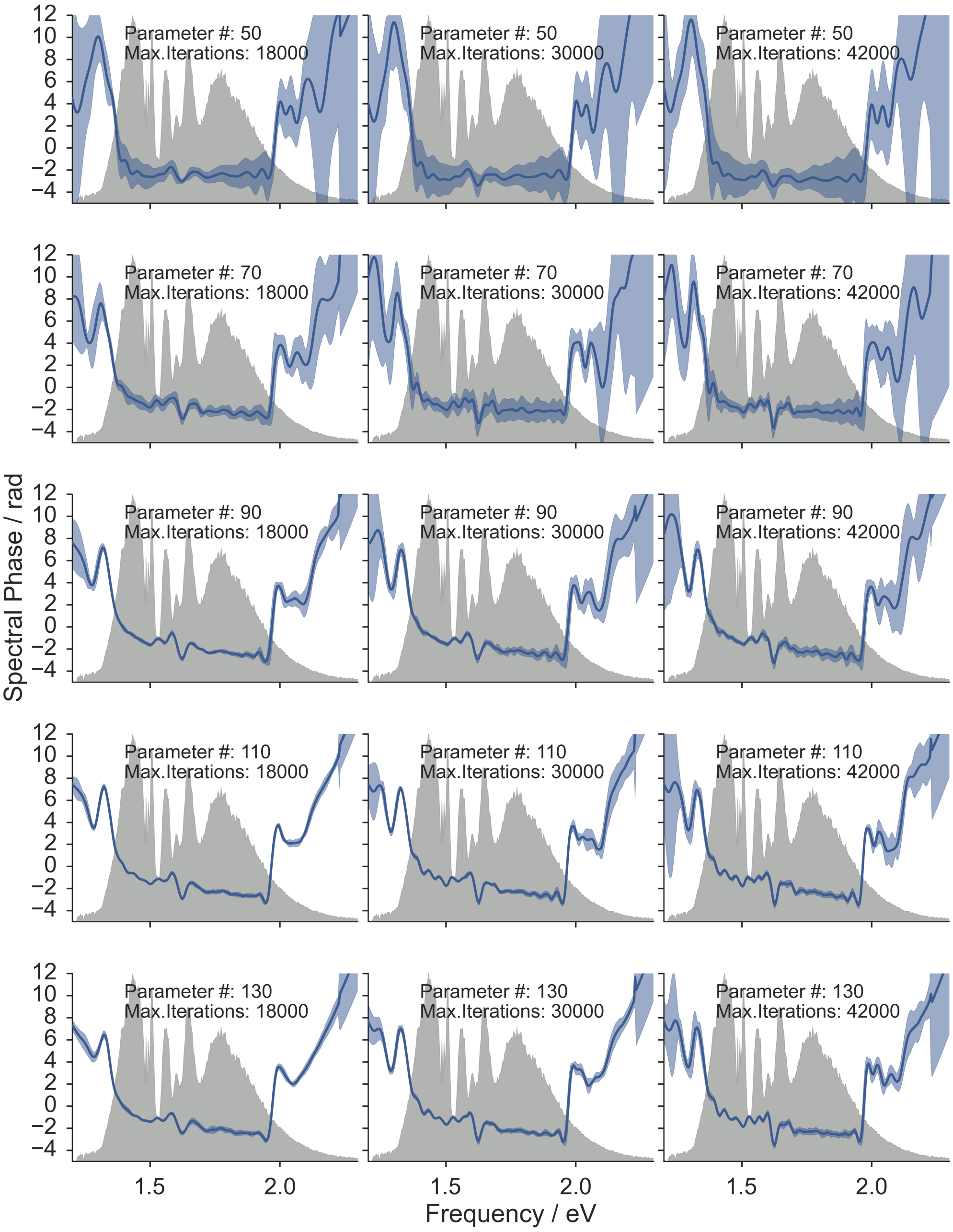

Figure A.2.: The same plots as in figure 3.8, with the difference that the measured data was sampled with half the number of steps in the glass insertion axis.

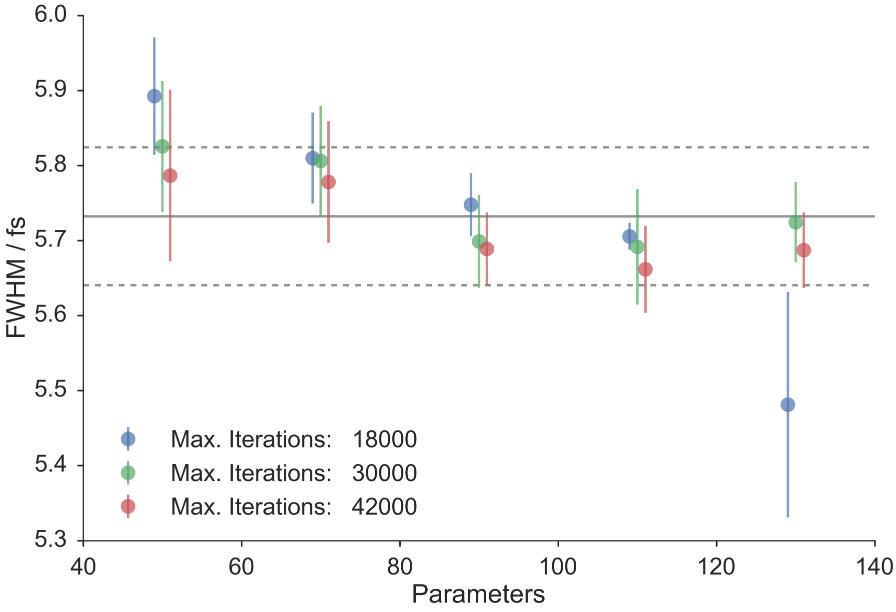

(a) FWHM data corresponding to figure A.1.

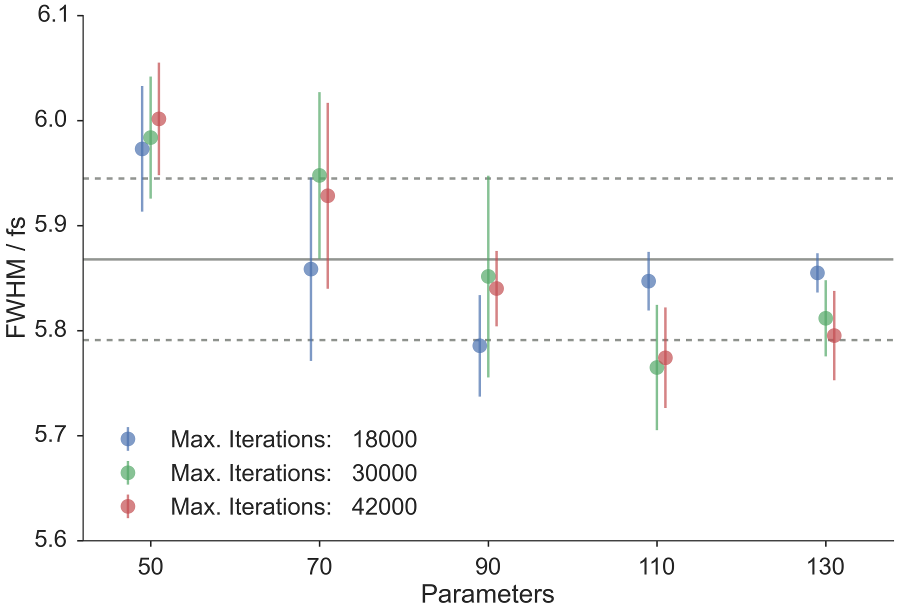

(b) FWHM data corresponding to figure A.2.

Figure A.3.: Full width at half maximum of the pulses, which are obtained from the spectral phases and amplitudes in the previous plots as a function of the number of parameters that built the phase functions and the number of iterations of the algorithm. The average of all values is indicated by the solid line with a confidence interval of one standard deviation (dashed lines).

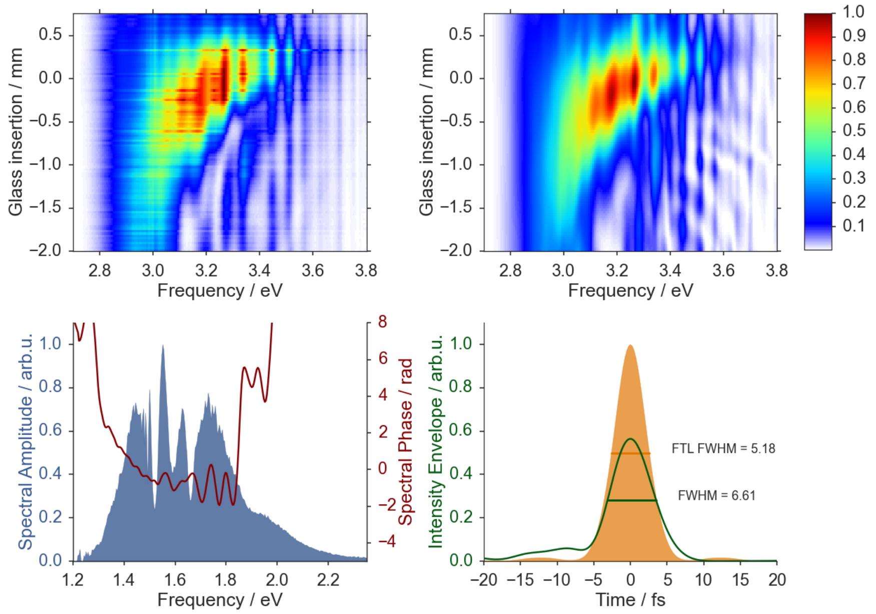

(a) Example of the D-Scan characterization of pulses with phase ripples and third order phase.

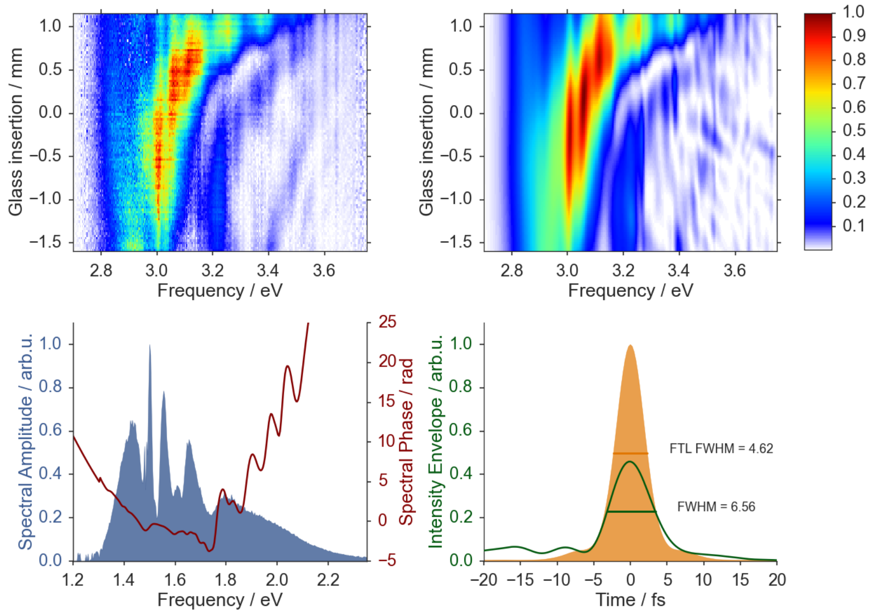

(b) Example of a very noisy D-Scan measurement.

Figure A.4.: On top are the experimental (left) and retrieved (right) traces. On the bottom, the spectral fields (left) and the temporal pulse envelopes (right) are shown.

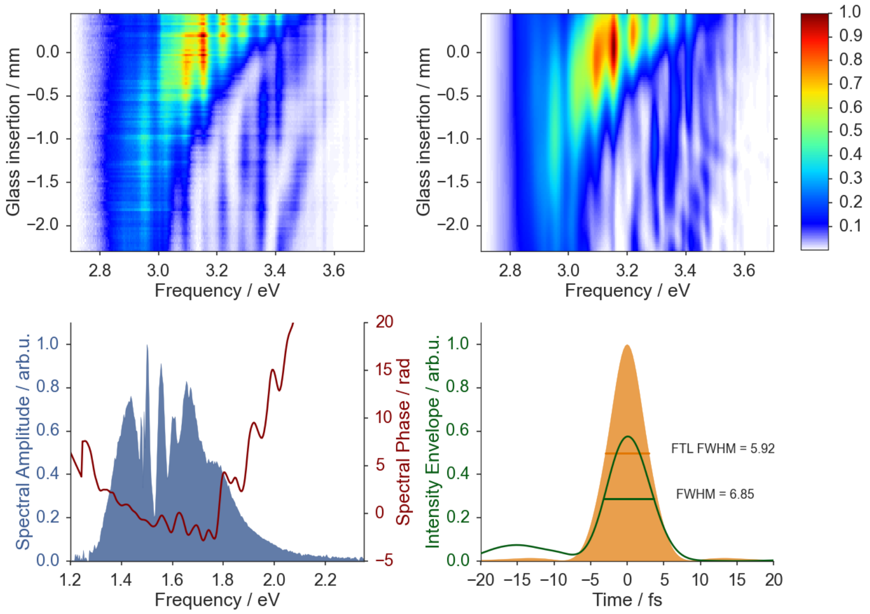

(a) Example of a D-Scan characterization.

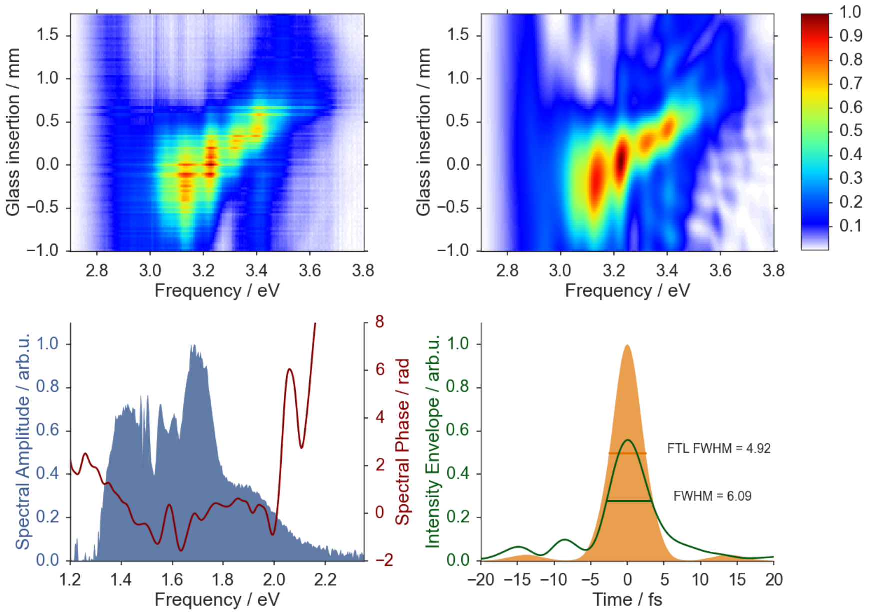

(b) Example of a D-Scan characterization.

Figure A.5.: On top are the experimental (left) and retrieved (right) traces. On the bottom, the spectral fields (left) and the temporal pulse envelopes (right) are shown.

Bibliography

[1] Blättermann, A., Ott, C., Kaldun, A., Ding, T., Stooß, V., Laux, M., Rebholz, M., and Pfeifer, T. (2015). In situ characterization of few-cycle laser pulses in transient absorption spectroscopy. *Opt. Lett.*, 40(15):3464–3467.

[2] Born, M. and Wolf, E. (1999). *Principles of optics: electromagnetic theory of propagation, interference and diffraction of light.* Cambridge university press.

[3] Bowlan, P., Gabolde, P., Shreenath, A., McGresham, K., Trebino, R., and Akturk, S. (2006). Crossed-beam spectral interferometry: a simple, high-spectral-resolution method for completely characterizing complex ultrashort pulses in real time. *Opt. Express*, 14(24):11892–11900.

[4] Chu, W.-C. and Lin, C. (2012). Photoabsorption of attosecond xuv light pulses by two strongly laser-coupled autoionizing states. *Phys. Rev. A*, 85(1):013409.

[5] Chung, J.-H. and Weiner, A. M. (2001). Ambiguity of ultrashort pulse shapes retrieved from the intensity autocorrelation and the power spectrum. *IEEE J. Quant. Electron.*, 7(4):656–666.

[6] Coello, Y., Lozovoy, V. V., Gunaratne, T. C., Xu, B., Borukhovich, I., Tseng, C.-h., Weinacht, T., and Dantus, M. (2008). Interference without an interferometer: a different approach to measuring, compressing, and shaping ultrashort laser pulses. *J. Opt. Soc. Am. B*, 25(6):A140–A150.

[7] Corkum, P. B. (1993). Plasma perspective on strong field multiphoton ionization. *Phys. Rev. Lett.*, 71(13):1994.

[8] DeLong, K. W. and Trebino, R. (1994). Improved ultrashort pulse-retrieval algorithm for frequency-resolved optical gating. *J. Opt. Soc. Am. A*, 11(9):2429–2437.

[9] Drescher, M., Hentschel, M., Kienberger, R., Tempea, G., Spielmann, C., Reider, G. A., Corkum, P. B., and Krausz, F. (2001). X-ray pulses approaching the attosecond frontier. *Science*, 291(5510):1923–1927.

[10] Eckle, P., Pfeiffer, A., Cirelli, C., Staudte, A., Dörner, R., Muller, H., Büttiker, M., and Keller, U. (2008a). Attosecond ionization and tunneling delay time measurements in helium. *Science*, 322(5907):1525–1529.

[11] Eckle, P., Smolarski, M., Schlup, P., Biegert, J., Staudte, A., Schöffler, M., Muller, H. G., Dörner, R., and Keller, U. (2008b). Attosecond angular streaking. *Nat. Phys.*, 4(7):565–570.

[12] Feng, X., Gilbertson, S., Khan, S. D., Chini, M., Wu, Y., Carnes, K., and Chang, Z. (2010). Calibration of electron spectrometer resolution in attosecond streak camera. *Opt. Express*, 18(2):1316–1322.

[13] Franken, P. A., Hill, A. E., Peters, C. W., and Weinreich, G. (1961). Generation of optical harmonics. *Phys. Rev. Lett.*, 7:118–119.

[14] Gao, F. and Han, L. (2012). Implementing the nelder-mead simplex algorithm with adaptive parameters. *Computational Optimization and Applications*, 51(1):259–277.

[15] Geiger, C. and Kanzow, C. (2013). *Numerische Verfahren zur Lösung unrestringierter Optimierungsaufgaben.* Springer-Verlag.

[16] Gilbertson, S., Chini, M., Feng, X., Khan, S., Wu, Y., and Chang, Z. (2010). Monitoring and controlling the electron dynamics in helium with isolated attosecond pulses. *Phys. Rev. Lett.*, 105(26):263003.

[17] Goodman, J. W. (2005). *Introduction to Fourier optics.* Roberts and Company Publishers.

[18] Goulielmakis, E., Schultze, M., Hofstetter, M., Yakovlev, V. S., Gagnon, J., Uiberacker, M., Aquila, A. L., Gullikson, E., Attwood, D. T., Kienberger, R., et al. (2008). Single-cycle nonlinear optics. *Science*, 320(5883):1614–1617.

[19] Goulielmakis, E., Uiberacker, M., Kienberger, R., Baltuska, A., Yakovlev, V., Scrinzi, A., Westerwalbesloh, T., Kleineberg, U., Heinzmann, U., Drescher, M., et al. (2004). Direct measurement of light waves. *Science*, 305(5688):1267–1269.

[20] Henke, B. L., Gullikson, E. M., and Davis, J. C. (1993). X-ray interactions: photoabsorption, scattering, transmission, and reflection at e= 50-30,000 ev, z= 1-92. *Atomic data and nuclear data tables*, 54(2):181–342.

[21] Hentschel, M., Kienberger, R., Spielmann, C., Reider, G. A., Milosevic, N., Brabec, T., Corkum, P., Heinzmann, U., Drescher, M., and Krausz, F. (2001). Attosecond metrology. *Nature*, 414(6863):509–513.

[22] Hoffmann, M., Nagy, T., Willemsen, T., Jupé, M., Ristau, D., and Morgner, U. (2014). Pulse characterization by thg d-scan in absorbing nonlinear media. *Opt. Express*, 22(5):5234–5240.

[23] Iaconis, C. and Walmsley, I. A. (1998). Spectral phase interferometry for direct electric-field reconstruction of ultrashort optical pulses. *Opt. Lett.*, 23(10):792–794.

[24] Itatani, J., Quéré, F., Yudin, G. L., Ivanov, M. Y., Krausz, F., and Corkum, P. B. (2002). Attosecond streak camera. *Phys. Rev. Lett.*, 88(17):173903.

[25] Jackson, J. D. (1962). *Classical electrodynamics*, volume 3. Wiley New York.

[26] Jiménez-Galán, Á., Argenti, L., and Martín, F. (2014). Modulation of attosecond beating in resonant two-photon ionization. *Phys. Rev. Lett.*, 113(26):263001.

[27] Kane, D. J. and Trebino, R. (1993a). Characterization of arbitrary femtosecond pulses using frequency-resolved optical gating. *IEEE J. Quant. Electron.*, 29(2):571–579.

[28] Kane, D. J. and Trebino, R. (1993b). Single-shot measurement of the intensity and phase of an arbitrary ultrashort pulse by using frequency-resolved optical gating. *Opt. Lett.*, 18(10):823–825.

[29] Kienberger, R., Goulielmakis, E., Uiberacker, M., Baltuska, A., Yakovlev, V., Bammer, F., Scrinzi, A., Westerwalbesloh, T., Kleineberg, U., Heinzmann, U., et al. (2004). Atomic transient recorder. *Nature*, 427(6977):817–821.

[30] Kornelis, W., Biegert, J., Tisch, J., Nisoli, M., Sansone, G., Vozzi, C., De Silvestri, S., and Keller, U. (2003). Single-shot kilohertz characterization of ultrashort pulses by spectral phase interferometry for direct electric-field reconstruction. *Opt. Lett.*, 28(4):281–283.

[31] Kosik, E. M., Radunsky, A. S., Walmsley, I. A., and Dorrer, C. (2005). Interferometric technique for measuring broadband ultrashort pulses at the sampling limit. *Opt. Lett.*, 30(3):326–328.

[32] Krausz, F. and Ivanov, M. (2009). Attosecond physics. *Rev. Mod. Phys.*, 81(1):163.

[33] Lozovoy, V. V., Pastirk, I., and Dantus, M. (2004). Multiphoton intrapulse interference. iv. ultrashort laser pulse spectral phase characterization and compensation. *Opt. Lett.*, 29(7):775–777.

[34] Mairesse, Y. and Quéré, F. (2005). Frequency-resolved optical gating for complete reconstruction of attosecond bursts. *Phys. Rev. A*, 71(1):011401.

[35] MATLAB (2013). Matlab and statistics toolbox release 2013b, the mathworks, inc., natick, massachusetts, united states.

[36] Miranda, M., Arnold, C. L., Fordell, T., Silva, F., Alonso, B., Weigand, R., L'Huillier, A., and Crespo, H. (2012a). Characterization of broadband few-cycle laser pulses with the d-scan technique. *Opt. Express*, 20(17):18732–18743.

[37] Miranda, M., Fordell, T., Arnold, C., L'Huillier, A., and Crespo, H. (2012b). Simultaneous compression and characterization of ultrashort laser pulses using chirped mirrors and glass wedges. *Opt. Express*, 20(1):688–697.

[38] Muller, H. . G. (2002). Reconstruction of attosecond harmonic beating by interference of two-photon transitions. *Appl. Phys. B*, 74(1):s17–s21.

[39] Nelder, J. A. and Mead, R. (1965). A simplex method for function minimization. *Comput. J.*, 7(4):308–313.

[40] Nicholson, J., Omenetto, F., Funk, D., and Taylor, A. (1999). Evolving frogs: phase retrieval from frequency-resolved optical gating measurements by use of genetic algorithms. *Opt. Lett.*, 24(7):490–492.

[41] O'Shea, P., Kimmel, M., Gu, X., and Trebino, R. (2001). Highly simplified device for ultrashort-pulse measurement. *Opt. Lett.*, 26(12):932–934.

[42] Ott, C., Kaldun, A., Argenti, L., Raith, P., Meyer, K., Laux, M., Zhang, Y., Blättermann, A., Hagstotz, S., Ding, T., et al. (2014). Reconstruction and control of a time-dependent two-electron wave packet. *Nature*, 516(7531):374–378.

[43] Pfeiffer, A. N., Cirelli, C., Smolarski, M., Dimitrovski, D., Abu-Samha, M., Madsen, L. B., and Keller, U. (2012). Attoclock reveals natural coordinates of the laser-induced tunnelling current flow in atoms. *Nat. Phys.*, 8(1):76–80.

[44] Pfeiffer, A. N., Cirelli, C., Smolarski, M., and Keller, U. (2013). Recent attoclock measurements of strong field ionization. *Chem. Phys.*, 414:84–91.

[45] Schultze, M., Fieß, M., Karpowicz, N., Gagnon, J., Korbman, M., Hofstetter, M., Neppl, S., Cavalieri, A. L., Komninos, Y., Mercouris, T., et al. (2010). Delay in photoemission. *Science*, 328(5986):1658–1662.

[46] Schultze, M., Goulielmakis, E., Uiberacker, M., Hofstetter, M., Kim, J., Kim, D., Krausz, F., and Kleineberg, U. (2007). Powerful 170-attosecond xuv pulses generated with few-cycle laser pulses and broadband multilayer optics. *New J. Phys.*, 9(7):243.

[47] Steinmeyer, G. (2003). Dispersion oscillations in ultrafast phase-correction devices. *IEEE J. Quant. Electron.*, 39(8):1027–1034.

[48] Strickland, D. and Mourou, G. (1985). Compression of amplified chirped optical pulses. *Opt. Commun.*, 55(6):447–449.

[49] Trebino, R. and Kane, D. J. (1993). Using phase retrieval to measure the intensity and phase of ultrashort pulses: frequency-resolved optical gating. *J. Opt. Soc. Am. A*, 10(5):1101–1111.

[50] Wang, H., Chini, M., Chen, S., Zhang, C.-H., He, F., Cheng, Y., Wu, Y., Thumm, U., and Chang, Z. (2010). Attosecond time-resolved autoionization of argon. *Phys. Rev. Lett.*, 105(14):143002.

[51] Wickenhauser, M., Burgdörfer, J., Krausz, F., and Drescher, M. (2005). Time resolved fano resonances. *Phys. Rev. Lett.*, 94(2):023002.

[52] Xu, B., Gunn, J. M., Cruz, J. M. D., Lozovoy, V. V., and Dantus, M. (2006). Quantitative investigation of the multiphoton intrapulse interference phase

scan method for simultaneous phase measurement and compensation of femtosecond laser pulses. *J. Opt. Soc. Am. B*, 23(4):750–759.

[53] Zhao, Z. and Lin, C. (2005). Theory of laser-assisted autoionization by attosecond light pulses. *Phys. Rev. A*, 71(6):060702.

[54] Zielinski, A., Majety, V. P., Nagele, S., Pazourek, R., Burgdörfer, J., and Scrinzi, A. (2015). Anomalous fano profiles in external fields. *Phys. Rev. Lett.*, 115(24):243001.

Aknowledgements

I would like to thank all members of the Interatto/X-MuSIC group: I learned a lot from you and enjoyed the friendly working atmosphere.
Special thanks go to …

Prof. Dr. Thomas Pfeifer who welcomed me to the Interatto/X-MuSIC group and gave me the great opportunity to work in the ultrafast community.
Priv. Doz. Dr. Alexander Dorn who kindly agreed to be the second reviewer of this thesis and shared his expertise on electron detectors.
Alexander Blättermann—without him this thesis would not be as it is. I thank him for answering all my questions, teaching me the ways of the white mungoose and the proof reading of this work.
Paul Birk for the weeks we spent together in the laboratory and for his unwavering critizism.
Martin Laux for answering my questions concerning time-of-flight experiments and high-voltage applications.
My office mates **Marc Rebholz** and **Lennart Aufleger** for having a bad influence on me. I am also grateful for the proof reading Marc did and the Labview skills Lennart taught me.
Veit Stooß and **Thomas Ding** for sharing their knowledge and experience.
Dr. Kristina Meyer and **Dr. Andreas Kaldun** who always had an open ear.
Mr. Weber from the construction team for working out the details of the electron spectrometer.
Matthias Brucklacher for bringing my servo shutters into existence.

For taking me as I am, calming the storms of my mind and rubbing the stress out of my back, I humbly admire Lia Oberhauser.
Last but not least, some special thanks go to my parents. Without their on-going trust and support none of the thesis would have been possible.

Erklärung:

Ich versichere, dass ich diese Arbeit selbstständig verfasst, und keine anderen als die angegebenen Quellen und Hilfsmittel benutzt habe.

Heidelberg, den 27. Januar 2016 ....

Declaration:

I hereby certify that the thesis I am submitting is entirely my own original work except where otherwise indicated.

Heidelberg, January 27th 2016 ....